1 **High-precision atmospheric oxygen measurement comparisons between a newly built**

2 **CRDS analyzer and existing measurement techniques**

4 Tesfaye A. Berhanu[1,2], John Hoffnagle[2], Chris Rella[2], David Kimhak[2], Peter Nyfeler[1], Markus

5 Leuenberger[1]

6 [1]*Climate and Environmental Physics, Physics Institute and Oeschger Centre for Climate Change Research,*

7 *University of Bern, Bern, Switzerland*

8 [2]*Picarro Inc., 3105 Patrick Henry Drive, Santa Clara, CA, USA*

10 **Abstract**

11 Carbon dioxide and oxygen are tightly coupled in land-biospheres CO_2 - O_2 exchange

12 processes, while they are not coupled in oceanic exchange. For this reason, atmospheric

13 oxygen measurements can be used to constrain the global carbon cycle, especially oceanic

14 uptake. However, accurately quantifying the small (~1-100 ppm) variations in O_2 is

15 analytically challenging due to the very large atmospheric background which constitutes

16 about 20.9 % (~209500 ppm) of atmospheric air. Here we present a detailed description of the

17 analyzer and its operating principles as well as comprehensive laboratory and field studies for

18 a newly developed high-precision oxygen mixing ratio and isotopic composition analyzer

19 (Picarro G-2207) that is based on cavity ring-down spectroscopy (CRDS). From the

20 laboratory tests, we have calculated a short-term precision (standard error of one-minute O_2

21 mixing ratio measurements) of < 1 ppm for this analyzer based on measurements of eight

22 standard gases analyzed for two hours consecutively. In contrast to the currently existing

23 techniques, the instrument has an excellent long-term stability and therefore a calibration

24 every 12 hours is sufficient to get an overall uncertainty of < 5 ppm. Measurements of

25 ambient air were also conducted at the High-Altitude Research Station, Jungfraujoch and the

26 Beromünster tall tower in Switzerland. At both sites, we observed opposing and diurnally

27 varying CO_2 and O_2 profiles due to different processes such as combustion, photosynthesis

28 and respiration. Based on the combined measurements at Beromünster tower, we determined

29 height dependent $O_2:CO_2$ oxidation ratios varying between -0.98 to -1.60 , which increase

30 with the height of the tower inlet, possibly due to different source contribution such as natural

31 gas combustion with high oxidation ratio and biological processes which are at the lower end.

1. Introduction

33 Atmospheric oxygen comprises about 20.9 % of the global atmosphere and in the past decade

34 its concentration decreased at a rate of $\sim$ 20 per meg yr^{-1} (Keeling and Manning, 2014) mainly

35 associated with the increase in fossil fuel combustion. Measurements of atmospheric O_2 are

36 reported as the ratio to the N_2 concentration and expressed as $\delta(O_2/N_2)$ because the variations

37 in the concentrations of other atmospheric gases such as CO_2 can influence the O_2 partial

38 pressure while this ratio is insensitive to these changes in other gases. Atmospheric O_2 is

39 commonly expressed in units of per meg due to its small variability with respect to a large

40 background, where

$$41 \quad \delta\left(\frac{O_2}{N_2}\right)(per\ meg) = \left(\frac{(\frac{O_2}{N_2})sample}{(\frac{O_2}{N_2})reference} - 1\right).10^6 \quad\quad (1)$$

43 Equation 1 is used to convert oxygen mole fraction changes expressed in ppm (as measured

44 by several techniques such as paramagnetic cell, UV-cell as well as the by the CRDS analyzer

45 presented here) into changes in $\delta O_2/N_2$. This is associated with the influence of dilution

46 effects on the mole fractions but not necessarily on the ratios. These conversion difficulties

47 and their expressions in uncertainties are discussed in the Appendix.In contrast to O_2, the

global average atmospheric CO_2 mixing ratio increased to 405.0 ppm averaged over 2017

since its preindustrial value of 280 ppm (Le Quéré et al., 2017). As the variability of

atmospheric oxygen is directly linked to the carbon cycle, both its short and long-term

observations can be used to better constrain the carbon cycle. For example, since first

suggested by Keeling and Shertz (1992) the long-term trends derived from concurrent

measurements of atmospheric CO_2 and O_2 have been widely used to quantify the partitioning

of atmospheric CO_2 between the land-biosphere and oceanic sinks (Battle et al., 2000; Goto et

al., 2017; Manning and Keeling, 2006; Valentino et al., 2008). This method hinges on the

linear coupling between CO_2 and O_2 with an oxidation ratio (OR, defined as the

stoichiometric ratio of exchange during various process such as photosynthesis and respiration

expressed using α) of 1.1 for the terrestrial biosphere photosynthesis-respiration processes

($α_b$) and 1.4 for fossil fuel combustion ($α_f$) while they are decoupled for oceanic processes ($α_o$

= 0). Meanwhile, the short-term variability in atmospheric oxygen can be used to estimate

marine biological productivity and air-sea gas exchange (Keeling et al., 1998; Nevison et al.,

2012). However, the accuracy of these estimates is primarily linked to the accuracy and

precision of atmospheric O_2 measurements and the assumed ORs for the different processes

which are highly variable in contrast to atmospheric CO_2 that can be well measured within the

precision guidelines set by the Global Atmospheric Watch (GAW) (± 0.1 ppm for the

northern hemisphere).

Currently there are several, mostly custom built techniques that can measure

atmospheric O_2 variations as oxygen concentration based on interferometric, paramagnetic,

UV absorption and fuel cell technology (Keeling, 1988a; Manning et al., 1999; Stephens et

al., 2007) or as O_2/N_2 ratios to account for the large background effect using gas

chromatography with thermal conductivity detector (GC-TCD) or gas chromatography

72   coupled to mass spectrometry (GC-MS) (Bender et al., 1994; Tohjima, 2000). Despite the fact

73   that these techniques have been used for more than two decades, accurate quantification of

74   atmospheric oxygen variability remains challenging primarily because the small ppm-level

75   atmospheric oxygen signal rides on a ~ 210,000 ppm background, which places stringent

76   requirements on the precision and drift of the analysis methods especially for continuous

77   monitoring(note that the GAW recommendation for the measurement precision of O_2/N_2 is 2

78   per meg). The techniques listed above struggle to routinely achieve the necessary performance

79   for various reasons, including i) instability over time that requires frequent measurement

80   interruption for calibration, ii) measurement bias with ambient and sample temperature and/or

81   pressure, and/or iii) systematic errors in the measurement due to other atmospheric species.

82   Further, some techniques require the use of consumables and rely on high vacuum, which

83   complicates field deployment.

84   In this manuscript we describe a new high precision oxygen concentration and isotopic

85   composition analyzer by Picarro Inc., Santa Clara, USA (G-2207) based on CRDS

86   technology. Here, we will introduce the analyzer design principles in details, describe the

87   unique features of the analyzer and evaluate its performance based on various independent

88   laboratory and field tests by comparing it with currently existing techniques. Then, we will

89   present and interpret our observations based on field measurements. Finally, we will conclude

90   its overall performance and provide recommendations and possible improvements.

91   **2. Analyzer design principles**

92   The analyzer described here is derived from the Picarro G2000 series of CRDS

93   analyzers. The basic elements have been described elsewhere (Crosson, 2008; Martin et al.,

94   2016; Steig et al., 2014): briefly, the instrument is built around a high-finesse, traveling-wave

95   optical cavity, which is coupled to either of two single-frequency Distributed FeedBack-

96 stabilized semiconductor lasers. One cavity mirror is mounted on a piezoelectric translator

97 (PZT) to allow fine tuning of the cavity resonance frequencies. A semiconductor optical

98 amplifier between the laser sources and the cavity boosts the laser power and serves as a fast-

99 optical switch. The cavity body is constructed of invar and enclosed in a temperature

100 stabilized box (T = 45° C, stabilized to approximately 0.01 °C) for dimensional and

101 spectroscopic stability. A vacuum pump pulls the gas to be sampled through the cavity and a

102 proportional valve between the cavity and the pump maintains the sample pressure in the

103 cavity at a value of 340 hPa, with variations on the order of 1 Pa. The instrument has a

104 wavelength monitor, based upon measurements of interference fringes from a solid etalon,

105 which is used to control the laser wavelength by adjusting the laser temperature and current.

106 The wavelength monitor is a fiber-coupled device located between the laser and the cavity. A

107 fraction of the beam from the input fiber is collected using a beam splitter for the wavelength

108 measurement and the remaining power is collected in the output fiber. A high-speed

109 photodiode monitors the optical power emerging from the cavity. The instrument's data

110 acquisition system is used to sweep the laser frequency over the spectral feature to be

111 measured, modulates the laser output to initiate ring-downs, and fits the ring-down signal to

112 an exponential function to generate a spectrogram of optical loss versus laser frequency. For

113 this instrument the empty cavity ring-down time constant is about 39 μs. Subsequent program

114 modules compare the measured loss spectrum to a spectral model, using non-linear least-

115 squares fitting (Press et al., 1986) to find the best-fit model parameters and thereby obtain a

116 quantitative measure of the absorption due to the target molecule, and finally apply a

117 calibration factor to the optical absorption to deduce the molecular concentration. When

118 operating in its normal gas analysis mode, the instrument acquires about 200-300 ring-downs

119   per second and achieves a noise equivalent absorption of typically about 10^{-11} cm^{-1} Hz$^{-1/2}$,

120   with some variation between instruments.

121   The primary goal when designing this analyzer was to measure the molecular oxygen

122   concentration with few-per-meg level precision and stability. In this context operational

123   stability is as important as signal-to-noise. Our experience has been that the most stable

124   operation of the analyzer is achieved when the optical phase length of the cavity is held as

125   nearly constant as possible. In this case the free spectral range (FSR, 0.0206 cm^{-1}) of the

126   temperature stabilized, invar ring-down cavity provides a better optical frequency standard

127   than the etalon-based wavelength monitor, which in turn allows more consistent

128   measurements of absorption line width and integrated absorption line intensity (Steig et al.,

129   2014). For a small, field-deployable instrument, it is not practical to stabilize the absolute

130   frequencies of the cavity modes to an optical frequency standard (Hodges et al., 2004) but the

131   oxygen lines themselves, under conditions of constant temperature and pressure, provide an

132   adequate frequency reference. The oxygen spectrum was also used to calibrate the FSR, by

133   comparing a wide (approximately 10 cm^{-1}) FSR-spaced spectrum with the Hitran database

134   (Rothman et al., 2013).

135   To determine molecular oxygen concentration, the analyzer measures absorption of the

136   Q13Q13 component of the $a^1\Delta_g \leftarrow X^3\Sigma^-_g$ band, at 7878.805547 cm^{-1}, according to the latest

137   edition of Hitran (Gordon et al., 2017). This is one of the strongest near-infrared lines of

138   oxygen, well separated from other oxygen lines, and reasonably free of spectral interference

139   from water, carbon dioxide, methane, and other constituents of clean air. The spectral model

140   for this line was developed using reference spectra of clean, dry, synthetic air that were

141   acquired with the same hardware as in the field-deployable analyzer, but with special-purpose

142   software that allows it to operate as a more general spectrometer.

143   Recently, considerable work has been done to advance the understanding of spectral

144   line shapes and to define functional representations that better describe the processes that

145   determine spectral line shapes than does the Voigt model (Hartmann et al., 2008; Tennyson et

146   al., 2014, Tran et al., 2019). Line shape studies have been published for the 1.27 μm band of

147   O_2 (Fleisher et al., 2015; Lamouroux et al., 2014), though not to our knowledge for the Q

148   branch. The apparatus used here is not capable of spectroscopic studies of comparable

149   precision; the absolute temperature and pressure monitoring and especially the frequency

150   metrology are far too crude for that purpose. Our goal is merely to define a simple model of

151   the Q13Q13 line that is adequate for least-squares retrievals of the O_2 absorption under the

152   limited range of conditions (stabilized temperature and pressure) that the operational analyzer

153   experiences in the field. The CRDS analyzers use the Galatry function (Varghese and Hanson,

154   1984), which is distinctly better than the Voigt and still easily and quickly evaluated for line

155   shape modeling. Ultimately, the usefulness of the spectral model is to be evaluated by the

156   precision and stability of the O_2 measurements when compared with established techniques.

157   For spectral model development, this spectrometer has the drawback that the cavity FSR, is

158   too large to reveal much detail of the absorption line shape, even with the simplifying

159   assumption of a Galatry line shape. We therefore acquired a set of four interleaved spectra,

160   with the PZT-actuated mirror moved to offset the cavity modes of the individual FSR-spaced

161   spectra by one-fourth of an FSR. The precise offsets were determined from fits to the strong

162   and well-isolated O_2 lines in the spectra. From the consistency of the fitted line centers, we

163   estimate that the positioning of the interleaved spectra was accurate to approximately 10

164   MHz. The spectrum of the Q13Q13 line acquired in this manner is shown in Figure 1,

165   together with the best-fit Galatry function. It stands out that the residuals are largely odd in

166   detuning from the line center: this shows the limitations of the Galatry model in this case,

167 since the Galatry function is purely even about the line center. The shape of the absorption

168 line in this model is specified by two dimensionless parameters: the collisional broadening

169 parameter

170 $y = \gamma / \sigma_D$ (2)

171 and the collisional narrowing parameter

172 $z = \beta / \sigma_D$ (3)

173 where γ is the frequency of broadening transitions, β is the velocity change collision rate, and

174 σ_D is the 1/e Doppler half-width of the transition, given by

175 $\sigma_D = \nu_0 (2k_B T / Mc^2)^{1/2}$ (4)

176 where ν_0 is the transition frequency, k_B is Boltzmann's constant (J. K^{-1}), T is the sample

177 temperature (K), M is the molecular mass (amu), and c is the speed of light (m/s). Figure 2

178 shows the values of y and z obtained from spectra acquired in the same way as Figure 1, as a

179 function of cavity pressure. The values depend linearly on pressure, as expected from the

180 Galatry model, but the unconstrained linear fits do not go precisely through the origin. It is

181 not clear whether this represents a breakdown of the Galatry model or simply reflects the

182 limited quality of the data set. The slope of y can be converted to an air-broadened collisional

183 width $\gamma_{air} = 0.0442$ cm^{-1}/atm, which agrees with the Hitran value of 0.0460 cm^{-1}/atm (Gordon

184 et al., 2016) to within the uncertainty estimate stated by Hitran (uncertainty code 4 for γ_{air}

185 corresponding to 10% --20% relative uncertainty). The slope of z can be interpreted in terms of

186 the optical diffusion coefficient (Fleisher et al., 2015), yielding D = 0.285 cm^2 s^{-1}, compared

187 to the literature value of 0.233 cm^2 s^{-1} for O_2 in air at 45 °C (Marrero and Mason, 1972).

188 Although the anticipated use of the analyzer is for ambient air samples having a very small

189 range of O_2 concentrations, we did investigate the variation of the line shape in binary

190 mixtures of O_2 and N_2 shown in Figure 3. The error bars are taken from the output of the

191 Levenberg-Marquardt fitting routine (Press et al., 1992). The dependence of the collisional

192 broadening parameter z on O_2 mole fraction was considered too small to be significant, but

193 the variation in y was used in the subsequent analysis of the air samples. Note that Wójtewicz

194 et al. (Wójtewicz et al., 2014) also found collisional broadening coefficients for nitrogen to be

195 slightly larger than for oxygen in measurements of one O_2 line in the B-band.

196   The primary goal in designing the analyzer was to achieve high enough precision to

197 make meaningful measurements of O_2 in clean atmospheric samples. Although the current

198 best practice for such high-precision measurements is to work with dried samples, we decided

199 to include high precision measurements of water vapor. There were two reasons for this

200 decision: one is to serve as a monitor for residual water vapor, which is difficult to remove

201 completely from the ring-down cavity and associated sample handling hardware, and the

202 second and more ambitious reason was to see how well the effect of water vapor could be

203 corrected for measurements of undried ambient air. While it was considered unlikely that

204 measurements of undried air could compete in accuracy with those of dried air, it might be

205 possible to correct for water vapor well enough to enable useful measurements in some

206 circumstances without the expense and inconvenience of drying the sample. For this purpose,

207 a second laser was added, which probes the $7_{1,6} \rightarrow 8_{4,5}$ component of the $2v_3$ band of water

208 vapor, at of 7816.75210 cm^{-1} (Gordon et al., 2017). The Galatry model was used to fit spectra

209 of synthetic air humidified to various levels of water vapor concentration. These fits also

210 included two other nearby, very weak water lines, with intensities less than 1% of the strong

211 transition, in order that their absorption should not perturb the line shape of the main

212 transition. Results for the shape of the 7816.75210 cm^{-1} line are shown in Figure 4. At the

213 level that we can measure, only the y-parameter has a meaningful variation with water

214 concentration. From the linear fit one obtains a pressure broadening coefficient for air, $\gamma_{air} =$

215   0.0752 cm^{-1}/atm, in reasonable agreement with the Hitran value γ_{air} = 0.0787 cm^{-1}/atm

216   (Gordon et al., 2017), and a self-broadening coefficient γ_{self} = 0.413 cm^{-1}/atm, to be compared

217   with the Hitran value γ_{self} = 0.366 cm^{-1}/atm. Since the uncertainty estimate for the Hitran

218   values is 10 % to 20 %, this level of agreement seems reasonable.

219   We also looked at absorption from water near the Q13Q13 absorption line of O_2.

220   These spectra were measured in a background of pure nitrogen to reveal the very weak lines

221   interfering with the O_2 measurement. Without the strong O_2 lines, it was impossible to

222   interleave FSR-spaced spectra, so in this case the frequency axis comes from the analyzer's

223   wavelength monitor. The upper panel of Figure 5 shows the spectrum of saturated water vapor

224   in nitrogen, together with a fit to a Voigt model of the molecular lines. The measurement was

225   made at a pressure of 340 hPa and temperature of 45° C. The main features are the Q13Q13 line

226   from trace contamination of oxygen in the sample and several lines that arise from normal water

227   ($^1H_2^{16}O$) and deuterated water ($^1H^2H^{16}O$ also abbreviated HDO). The lower panel of Figure 5 shows

228   the lines tabulated in Hitran. Immediately after the data in Figure 5 were acquired,

229   measurements were also made at 7816.85210 cm^{-1}, to establish the relationship between the

230   absorption strengths in the two spectral regions. The relative intensities of the H_2O and HDO

231   lines change with variations in the isotopic composition of the water, but fortunately the direct

232   interference with the oxygen Q13Q13 lines comes entirely from the H_2O isotopologue, with

233   the strongest HDO line being separated by approximately 8 line widths (FWHM) from the

234   Q13Q13 line. Hitran simulations for molecules other than water that are expected to be

235   present in clean, ambient air indicate that direct interference with the Q13Q13 line should be

236   negligible at the level of precision considered here. In the case of CO_2, the dilution of oxygen

237   due to 400 ppm of CO_2 is significant, and larger than any direct spectral interference.

238   Finally, we investigated the influence of water vapor on the shape of the O_2 Q13Q13

239   line. Switching between the two lasers sources, we acquired FSR-spaced spectra of

240   humidified synthetic air, alternately covering the 7817 cm^{-1} and 7878 cm^{-1} regions. Individual

241   spectra were acquired in less than 2 s, so changes in water vapor concentration between

242   spectra were small. These spectra, with frequency resolution of 0.0206 cm^{-1}, were analyzed by

243   nonlinear least-squares fitting with the following spectral models: the 7817 cm^{-1} spectra were

244   modeled as the sum of an empty-cavity baseline having an adjustable offset level and slope

245   and the water spectrum is modeled with three peaks: one strong line and two weak perturbers.

246   The molecular absorption of the main peak was expressed as an adjustable amplitude, A_w,

247   multiplying a dimensionless, area-normalized Galatry function (Varghese and Hanson, 1984).

248   The weak perturbers were modeled by Voigt profiles with amplitudes and line widths that

249   were constrained to be in fixed proportions to the strong line, and therefore added no new

250   degrees of freedom to the fitting procedure. Since the amplitude A_w multiplies an area-

251   normalized shape function, it is essentially equivalent to the area of the absorption line, to the

252   extent that the Galatry model provides a valid description of the line shape. The Doppler

253   width of the Galatry function was fixed based on the measured cell temperature, the y-

254   parameter was allowed to vary, and the z-parameter was constrained to be proportional to y,

255   based on measurements summarized in Figure 2. In addition, the center frequency of the

256   Galatry function was adjusted to match the data set, giving a total of five free parameters for

257   this fit. The 7878 cm^{-1} spectra were modeled with an adjustable baseline offset and slope and

258   molecular absorption amplitude, A_{O2}, describing the Q13Q13 O_2 line. Here, too, the y-

259   parameter and line center position of the O_2 lines were allowed to adjust, and the z-parameter

260   was constrained to be proportional to y. The weak water lines interfering with oxygen

261   absorption were included in the model, but with no additional free parameters; rather the

262 amplitudes were preset based on the measured water absorption at 7817 cm^{-1} and the

263 previously determined amplitude relationships between the water lines. This procedure does

264 not account for variations in HDO abundance, which may introduce some systematic error

265 into the water vapor correction for samples of unusual isotopic composition, but it should

266 accurately model the most important lines that interfere with the oxygen measurement.

267 Collisional broadening of the Q13Q13 O$_2$ line by water vapor is shown in Figure 6. From the

268 linear fit one obtains a coefficient for collisional broadening of the Q13Q13 line by water

269 vapor of γ_{water} = 0.0442 cm^{-1}/atm at 45 °C. Recently, parameters describing broadening of

270 oxygen lines by water vapor, obtained by empirical modeling of selected experimental

271 data, were added to the Hitran data base (Tan et al., In review). The new Hitran entries predict

272 a value of 0.0486 cm-1/atm at 45 °C, which is in agreement with our measurement within the

273 5-10% uncertainty attributed by Hitran to the broadening parameter. The alternating

274 measurements at 7817 cm^{-1} and 7878 cm^{-1} also calibrated the relationship between water mole

275 fraction and the absorption at 7817 cm^{-1}, using a dilution analysis described by Filges et al.

276 (2018), who showed that the results obtained this way agree well with water vapor fractions

277 measured with a conventional hygrometer. Figure 7 shows the measured amplitudes of the

278 water and oxygen lines for samples of variable humidity. Since the air came from a tank of

279 constant composition, the oxygen concentration changes due to dilution of oxygen when

280 water is added. Assuming that this is the sole cause of the change in measured absorption,

281 since the line shapes were being constantly adjusted to account for changes in collisional

282 broadening, it is straightforward to deduce the relation between the water fraction and the

283 absorption amplitude. This calibration was used to generate the water fraction axes in Figures

284 4 and 6. We note that we did not take particular care to control or measure the quantity of

285 dissolved gases, especially oxygen and carbon dioxide, in the water used for this experiment.

While these gases would not significantly affect the water calibration, they may affect the water vapor correction of the oxygen measurement at the ppm level. More work needs to be done to investigate the water vapor correction of the oxygen measurement.

The observations described above were used to design a method to measure oxygen concentration in ambient air. Gas from the inlet to the analyzer is drawn through the cavity at a rate of about 100 sccm (standard cubic centimeter per minute) and the conditions in the cavity are held stable at 340 hPa and 45°C. In its analysis mode the analyzer alternately measures ring-downs in the 7817 cm^{-1} and 7878 cm^{-1} regions. At 7878 cm^{-1} measurements are made at 11 different frequencies, spaced by one FSR of the cavity and centered at the peak of the Q13Q13 line. Multiple ring-down measurements are made to improve the precision of the loss determination, with a total of 305 ring-downs allocated to one spectrum. In the 7817 cm^{-1} region measurements are also made at 11 distinct frequencies at FSR spacings. Only 35 ring-downs are allocated to this spectral region, since the measurement of O_2 is much more important than water vapor. The data sets are analysed using a Levenberg-Marquardt fitting routine, which adjusts five free parameters in each region to find the best agreement to a spectral model based on Galatry line shapes, as described above. One of the outputs of the 7878 cm^{-1} fit is the frequency offset of the FSR grid from the center of the Q13Q13 line. This information is used to adjust the position of the PZT actuated mirror to keep the measurements centered on the line, effectively stabilizing the optical path length of the cavity to the frequency of the O_2 line. The reported water fraction is obtained by multiplying the fitted amplitude of the water line by a calibration constant derived from the dilution experiment as explained above. For the O_2 fraction a slightly more complicated procedure is followed. It was observed that the least-squares fitting of the data gives highly correlated results for the amplitude of the absorption line and the line width parameter y. The correlation

310   may be due in part to covariance of the fitted amplitude (proportional to line area) and line

311   width (Press et al., 1992) and it may also have a contribution from pressure variations that the

312   pressure sensor is unable to detect. The ratio A_{O2}/y can be determined from the fit much more

313   precisely than A_{O2} alone and so gives a more sensitive measurement of molecular absorption.

314   It also has the advantage of being independent of sample pressure, to the extent that the

315   Galatry model applies (Figure 2). However, using the ratio A_{O2}/y as a metric for absorption

316   adds more complications if measurements are to be made over a range of O_2 and water

317   concentrations, because the O_2/N_2 ratio and the water concentration affect the line width

318   independently of pressure and O_2 concentration alone. To minimize systematic errors due to

319   these broadening effects, we define a nominal y-parameter based on the measured amplitudes

320   of the O_2 and water lines and the line broadening dependences shown in Figures 3 and 4. The

321   measured ratio A_{O2}/y is multiplied by the nominal y to obtain a quantity that is ideally

322   independent of pressure and water concentration, and this is the quantity that is multiplied by

323   a calibration constant to give the reported O_2 fraction. In addition, a dry mole fraction is

324   reported for O_2, defined as the directly measured mole fraction corrected for water dilution.

325   The main goal in developing this instrument was to make high precision

326   measurements of O_2 mole fraction, based on absorption by the dominant $^{16}O_2$ isotopologue.

327   The absorption lines of the rarer isotopologues are also present nearby, so a mode of operation

328   was included in which one laser is scanned over neighboring lines of $^{16}O_2$ and $^{16}O^{18}O$ and the

329   ratio of amplitudes is used to derive an isotopic ratio, reported in the usual delta notation. In

330   this case the operating pressure was reduced to 160 hPa to improve the resolution of the

331   nearby lines. The lines measured were the Q3Q3 line of $^{16}O_2$, at 7882.18670 cm^{-1}, and the

332   Q9Q9 line of $^{16}O^{18}O$, at 7882.050155 cm^{-1}. The measurement procedure is very much like

333   that for the O_2 fraction measurement, so it will not be described in detail, only the main

334   differences will be noted. One is that in determining an isotopic ratio, normalizing absorption

335   amplitudes by line widths does not provide any advantage, instead we simply take the ratio of

336   amplitudes to compute delta. Although the Q9Q9 line and its neighbor Q8Q8 are the strongest

337   ones in this band, absorption by $^{16}O^{18}O$ is still very weak, only about $5x10^{-9}$ cm^{-1} at the line

338   center under the conditions we used. The signal-to-noise that can be achieved with this

339   analyzer is not adequate to determine both the amplitude and the width of the $^{16}O^{18}O$ line with

340   useful precision, so in the fitting step the y-parameter of the $^{16}O^{18}O$ line is constrained to be a

341   constant factor times the fitted y-parameter for the $^{16}O_2$ line. Additionally, because of the

342   weakness of the rare isotopologue absorption, the majority of ring-downs in each spectrum is

343   devoted to measuring $^{16}O^{18}O$ i.e. 232 ring-downs in each spectrum versus only 40 for $^{16}O_2$.

344   This implies that the mole fraction measurement in the isotopic mode is much less precise

345   than when the analyzer measures the Q13Q13 line alone.

346   **3. Results and Discussions**

347   **3.1. Laboratory tests at Picarro, Santa Clara**

348   3.1.1. Temperature and pressure sensitivity

349   One set of tests was done to determine how well the goal was met of minimizing the

350   susceptibility of the concentration measurements to noise or drift of the sample temperature

351   and pressure. For these tests the analyzer sampled dry synthetic air from a tank and the

352   temperature and pressure setpoints of the cavity were adjusted upward and downward from

353   the nominal values, to obtain an estimate of the differential response. We express the

354   sensitivity to experimental conditions in relative form, that is the derivative with respect to

355   temperature or pressure divided by the signal under nominal conditions.

356   From these experiments, we determined a temperature sensitivity of $-2.1x10^{-4}$ K^{-1} and

357   a pressure sensitivity of $+9.8x10^{-6}$ hPa^{-1}. The temperature sensitivity is somewhat larger than

expected based on a calculation using Hitran data to estimate the temperature dependences of all the quantities that go into the measured absorption of the Q13Q13 line. The pressure sensitivity is strikingly small, indicating a good cancelation of the pressure dependence of absorption amplitude and line width. Both temperature and pressure sensitivities are small enough to have a negligible effect on short-term precision of measurements made with the stabilized ring-down cavity, though long-term drifts in the sensors are always a matter of concern.

3.1.2. Measurement precision and drift

Measurement precision was evaluated by analyzing synthetic air containing nominal atmospheric concentrations of CO_2 and CH_4 from an aluminum Luxfer cylinder over a period of several days. The tank, oriented horizontally and thermally insulated (though not controlled), was connected directly to the instrument (S/N TADS2001) with a 2-stage pressure regulator and stainless-steel tubing with an additional orifice to about 55 sccm. For the isotopic mode of operation, the precision of the measurement was also tested by making repeated measurements from a tank of clean, dry synthetic air.

Figure 8 shows the time series of the precision test data, displaying the reported oxygen concentration, the height of the oxygen absorption peak, the width of the oxygen absorption peak and the ambient temperature. The residual error of the analyzer, although small, is nevertheless significant given the stringent targets set forth by the WMO-GAW program. Possible sources of error include: temperature drifts due to sensor drift or gradients; pressure errors due to sensor drift; optical artifacts such as parasitic reflections, higher order cavity mode excitation, and/or loss nonlinearity that can distort the reported oxygen spectrum. More work is required to identify and eliminate these small drifts.

381   The Allan standard deviation of the reported O_2 fraction is shown in the Allan-Werle

382   plot in Figure 9. The ordinate on this plot is the square root of the Allan variance of reported

383   mole fraction, so 1 ppm in these units corresponds to about 5 per meg in the ratio of O_2/N_2.

384   The precision of averaged measurements improves as $\tau^{-1/2}$ for approximately 5000 s and

385   reaches 1 ppm in less than 10 minutes and remains below 1 ppm for time scales on the order

386   of about 1 hour (τ is the averaging time which is the abscissa of the Allan-Werle plot).

387   Figure 10 shows the precision of $\delta(^{18}O)$ (uncalibrated) derived from the ratio of lines

388   measured at 7882 cm^{-1}. Because of the weak signal from the $^{16}O^{18}O$ line, it is necessary to

389   average for more than 20 seconds or more to achieve 1‰ precision on the isotopic ratio. As

390   for the concentration measurement, averaging improves the measurement precision for time

391   scales up to about 1 hour.

392   **3.2. Laboratory measurements at the University of Bern**

393   3.2.1. Measurements of standard gases

394   The performance of the instrument was tested by analyzing eight standard gases with

395   precisely known CO_2 and O_2 compositions (Table 1) using the CRDS analyzer and comparing

396   it to parallel measurements with a paramagnetic oxygen sensor (PM1155 oxygen transducer,

397   Servomex Ltd, UK) embedded to a commercially available fuel cell oxygen analyzer

398   (OXZILLA II, Sable Systems International, USA) (Sturm et al., 2006) as well as with an

399   isotope ratio mass spectrometer (IRMS, Finnigan Delta^{Plus}XP). The design of the

400   measurement set-up is shown in Figure 11. Standard gases were directly connected to the

401   pressure controlling unit, and a multi-port valve (V2) was used to select among the standard

402   gases. Flow from each cylinder was adjusted to about 120 sccm which was eventually

403   directed to a selection valve (V1), allowing switching between ambient air and standard gases.

404   Flow towards and out of the fuel cell analyzer was controlled by the pressure controlling unit.

405   The O_2 mixing ratio of this incoming gas was first measured on the Paramagnetic O_2 sensor

406   and then directed towards a non-dispersive infrared analyzer (NDIR) (Li-7000, LICOR, USA)

407   for measuring CO_2 and H_2O. The outflow from this analyzer (100 sccm) returns to the

408   pressure controlling unit and was eventually divided between the CRDS analyzer (which uses

409   about 75-80 sccm) and the IRMS (~ 20 sccm) via a Tee-junction. Each cylinder was measured

410   for two hours in each system controlled by a LabView program.

411   First, we investigated the influence of this Tee-junction, which splits the gas flow

412   between the CRDS and the IRMS, on the measured O_2 values. Manning (2001) showed that

413   the fractionation of O_2 in the presence of a Tee-Junction is strongly dependent on the splitting

414   ratios as well as temperature and pressure gradients. Hence, we measured and compared the

415   O_2 mixing ratios of two standard gases (CA07045 and CA060943) in two cases: i) in the

416   presence of a Tee-junction with different CRDS to IRMS splitting ratios and ii) without a

417   Tee-junction so that all gas flow is directed towards the CRDS analyzer. The splitting ratios in

418   these test experiments vary from 1:1 to 1:100, and reversed to change the major flow direction

419   either to the CRDS or the IRMS. Note that the experimental condition in this manuscript is

420   with a 4:1 splitting ratio (i.e. ~ 80 sccm towards the CRDS analyzer and ~ 20 sccm towards

421   the IRMS).

422   In the cases of the smaller splitting ratios (1:1, 1:4 and 4:1), which are relevant for the

423   results presented in this study, only minor differences in the measured O_2 mixing ratios were

424   observed when compared to case ii (i.e. without a Tee-junction). For these two cylinders

425   measured, the average differences in these cases were about 0.5 ppm, calculated as the mean

426   of the differences in the raw O_2 measurements of the last 60 seconds. The negligible

427   fractionation can indeed be the result of smaller splitting ratios while strong influence is

428   usually expected in case of larger splitting ratios (Stephens et al., 2007). For higher splitting

429   ratios, the result seems inconclusive without any dependence on the ratios due to the strong

430   decline in the cylinder temperature (specifically at the pressure gauge) caused by higher flow

431   to achieve the higher splitting ratios (as high as 1:100). Hence, these tests need to be

432   conducted in a temperature-controlled condition and the results could not be discussed in this

433   manuscript.

434   Figure 12 shows the standard gas measurements for the seven cylinders with known

435   CO_2 and O_2 mixing ratios (Table 1) using both the CRDS and the Paramagnetic analyzers.

436   Standard eight, which has too high O_2, is not shown in the figure as the figure is zoomed-in to

437   better illustrate the change in O_2 for the remaining cylinders. While the first five cylinders

438   contain O_2 and CO_2 mole fractions comparable to ambient air values, standards 6 & 8 had

439   either very low or very high O_2, respectively. In addition, standards 6 and 7 have very low and

440   very high CO_2 mixing ratios. Note that due to its very high CO_2 content (~ 2700 ppm),

441   standard 7 was not measured on the IRMS and hence the O_2 mixing ratio is unknown. The

442   measured mixing ratios for the six standard gases measured with the two systems are in very

443   good agreement while cylinder 7 showed an opposing signal for the two analyzers compared

444   to standard 6 (Figure 12). While the Paramagnetic analyzer showed a higher O_2 mixing ratio,

445   the values from the CRDS analyzer are lower in O_2. This can be associated with the very high

446   CO_2 mixing ratio in standard 7, which leads to a strong dilution effect in the CRDS analyzer

447   as it does not include any correction function for dilution effect from CO_2. However, such

448   high CO_2 mixing ratios may not be that important for most atmospheric research. Yet, it

449   should be considered to include a parallel CO_2 mixing ratios measurement to the instrument

450   as it will further improve the accuracy. This would be especially important for biological or

451   physiological studies where a wide range of CO_2 and O_2 concentrations must be expected.

452   The measurement precision of the CRDS analyzer was calculated as the standard error

453   of the mean i.e. the standard deviation (1-σ) of the last 1-minute raw measurements divided

454   by the square root of the number of measurements (n = 60), and for all these cylinders the

455   values are usually between 0.5 ppm to 0.7 ppm. For parallel measurements of these cylinders

456   using a Paramagnetic analyzer, we obtained a precision of about 1 ppm, calculated exactly the

457   same way.

458   We also made a correlation plot to see which of the two instruments are in better

459   agreement with the assigned values based on IRMS measurements for the individual

460   cylinders. While similar correlation coefficients were observed for both analyzers, different

461   slopes were calculated (Fig. A.1). This is due to the fact that the IRMS measures the O_2 to N_2

462   ratio ($\delta(O_2/N_2)$) in per meg, while the CRDS and the Paramagnetic analyzers provide non-

463   calibrated O_2 mixing ratios in units of ppm and per meg, respectively. If we exclude the two

464   standard gases with the highest and lowest O_2 mixing ratios (standards 7 and 8) that are

465   subjected to strong dilution effects, both the slope and the r^2 values decrease from those

466   shown in Figure A.1. But this decrease is larger in the case of the Paramagnetic

467   measurements, implying a slightly better linearity of the CRDS analyzer.

468   Furthermore, the slope between the IRMS and CRDS O_2 values in Figure A1

469   corresponds to 5.78 per meg ppm^{-1}, significantly larger than the conversion factor of 4.78 per

470   meg ppm^{-1} as derived from equation 1 assuming constant N_2 content. This higher slope is due

471   to dilution effect originating from any gas component change (Delta, given in ppm) on all air

472   components of air samples, which has not been corrected for the CRDS values. When

473   accounting for this dilution effect - which scales with 1/(1+Delta), the factor approaches 4.78

474   per meg ppm^{-1}. The scaling of dilution effects is independent on which air component is

475   changing and it affects all air components relative to their molecular fractions similarly. O_2

476 values on a CRDS or paramagnetic cell instrument is affected even if there is no change in O_2

477 or N_2 but only in CO_2 or water vapor or any other component which is present. This is in

478 contrast to measurements of O2/N2 ratios for the same case where equal ratio would be

479 measured. Major dilution influences are expected from O_2, CO_2 and H_2O changes due to

480 natural exchange processes on air samples or when using artificial air-like compositions.

481 3.2.2. Measurements of ambient air

482   Ambient air measurements were conducted from the roof top of our laboratory at the

483 University of Bern to evaluate the analyzer's performance under atmospheric variability.

484 Ambient air was continuously aspirated from the inlet at the roof of the building at a flow rate

485 of ~ 250 sccm which is then dried using a cooling trap kept at -90 °C towards the switching

486 valve (V1) and measured in similar way to the standard gases as explained above. The

487 measurement values obtained here were compared with the parallel measurements by the

488 Paramagnetic sensor to test the instruments stability and accuracy.

489   Figures 13 panels a &b show the 1-minute average ambient air measurements from the

490 rooftop inlet by the Paramagnetic and the CRDS analyzers at the beginning of the testing

491 period including standard gases measured every 12-hour. While the Paramagnetic analyzer

492 seems to be stable, the CRDS analyzer showed a strong drift for an extended period. This can

493 be due to unstable conditions in the CRDS measurement system as it started operating right

494 after it was unpacked. Hence, we looked into temperature inside the instrument chassis and

495 pressure records, which were stable within the manufacturer's recommended range during this

496 period. As the CRDS analyzer incorporates a water correction function, interference from this

497 species should be well accounted. Even comparing the analyzer's parallel water

498 measurements to water measurements by the NDIR system such a drift was not observed. It

499 should be noted that the two internal standard gases which were less frequently measured

500 (every 12 hours) during this period were also drifting following similar pattern. This implies

501 that the drift is associated with the analyzer. Interestingly, this pattern can be modeled using a

502 polynomial function which can then be used to correct for the observed drift in the ambient air

503 measurements. After applying a polynomial drift correction, we were able to fully accounted

504 for the observed drift. However, the manufacturer decided to further investigate possible

505 causes of this drift. After further improvements, we obtained the first commercial analyzer in

506 September 2017 and repeated the above tests (Figure 13 c &d). No such drift was observed

507 any more in the standard gases or in ambient air measurements.

508 We believe that the optical amplifier has caused the drift in the first system and not anymore

509 included in the design of the product which produced a significant amount of broadband light

510 that could fill the cavity (albeit with a low coupling coefficient), and would ring down with a

511 different (and generally much faster) time constant that the baseline loss of the cavity.

512 However, the ringdown time on the peak of the oxygen line is just 10 microseconds, such that

513 the broadband light might have distorted the single exponential decay of the central laser

514 frequency, leading to the observed drift in the oxygen signal. However, we were not able to

515 confirm this hypothesis.

516 3.2.3. Water correction test

517 Measurements of oxygen are reported as both wet ($O_{2, raw}$) and dry ($O_{2, dry}$) mole

518 fractions by the CRDS analyzer as it also measures water vapor in parallel at its water

519 absorption line (7817 cm^{-1}), and corrects for the dilution effect based on an inbuilt numerical

520 function:

521
$$O_{2,dry} = \frac{O_{2,raw}}{1-H_2O} \tag{5}$$

522 where H_2O is the measured water mole fraction.

523 The efficiency of water correction by this function was assessed in two ways: i) by comparing

524 the water vapor content in standard air measured by this analyzer with similar measurements

525 by the NDIR analyzer and ii) by comparing the oxygen mixing ratios between non-dried

526 ambient air measured and corrected for water dilution by the CRDS analyzer with dried air

527 measured using a paramagnetic analyzer.

528 Figure 14 shows the water vapor content for standard gases measured continuously for

529 two days by the CRDS and the NDIR analyzers. Note that the two data sets are manually

530 fitted to each other as the measured water values by the NDIR analyzer are not calibrated.

531 Based on this plot, the two analyzers are in very good agreement although there are small

532 differences during very dry conditions (low water content).

533 Figure 15a shows the dried ambient air water measurements in both analyzers with

534 frequent spikes due to valve switching while measuring standard gases. In the second case,

535 where the water trap was by-passed and non-dried air was allowed to the CRDS analyzer

536 keeping the dried air flow to the NDIR (Figure 15b), a clear increase in the water

537 measurements in the CRDS analyzer can be observed. Here, it should be noted that there are

538 no spikes in the water measurements of the CRDS analyzers as there are no standard gas

539 measurements in between and the inlet is directly connected to the CRDS analyzer (Figure

540 11). Figures 15c & 15d show the difference in oxygen measurements of ambient air measured

541 in both analyzers in the two cases stated above (note that the CRDS uses its built-in water

542 correction function applying Eq. 5). The measurements of the Paramagnetic analyzer were

543 scaled to ppm units by applying the correlation equation obtained from the six standard gas

544 measurements of the two analyzers (Fig. A.1). Note that the CRDS measurements were

545 corrected for the observed drift using the polynomial fit to the two standard gas measurements

546 stated above.

547   In the first period of the measurement when both analyzers measured dried ambient

548   air, the absolute differences between the 1-minute averages measured over two days by the

549   two analyzers were mostly within 15 ppm (Figure 15c) and symmetrically distributed around

550   zero (Figure 15e). However, when wet air was admitted to the CRDS analyzer and the in-built

551   water correction was applied, a stronger variability was observed in the calculated differences

552   (Figure 15d). This implies stronger short term variability in the CRDS analyzer measurement

553   values (as nothing was changed for the Paramagnetic measurement system) when wet samples

554   were analyzed. The more negative values in the differences (Figure 15f) can also be

555   associated with overestimation of the O_2 mixing ratios by the CRDS originating from an

556   overestimated water correction. However, detailed evaluation of the analyzer's water

557   correction function is beyond the scope of this study.

558   **3.3. Field Measurements**

559   After a series of tests at University of Bern, we conducted multiple field measurements

560   at the High Altitude Research Station Jungfraujoch and the Beromünster tall tower sites in

561   Switzerland described below.

562   3.3.1. Tests at the High Altitude Research station Jungfraujoch

563   The High Alpine research station Jungfraujoch is located on the northern ridge of the

564   Swiss Alps (46° 33′ N, 7° 59′ E) at an elevation of 3580 m a.s.l. It is one of the global

565   atmospheric watch (GAW) stations well-equipped for measurements of numerous species and

566   aerosols. The site is above the planetary boundary layer most of the time due to its high

567   elevation (Henne et al., 2010; Zellweger et al., 2003). However, thermally uplifted air from

568   the surrounding valleys during hot summer days or polluted air from the heavily industrialized

569   northern Italy may reach at this site (Zellweger et al., 2003). The Division of Climate and

570   Environmental Physics at the University of Bern has been monitoring CO_2 and O_2 mixing

571 ratios at this site based on weekly flask sampling and continuous measurements since 2000

572 and 2004, respectively (Schibig et al., 2015). The CO_2 mixing ratio is measured using a

573 commercial NDIR analyzer (S710 UNOR, SICK MAIHAK) while O_2 is measured using the

574 Paramagnetic sensor (PM1155 oxygen transducer, Servomex Ltd, UK) and fuel cells (Max-

575 250, Maxtec, USA) installed inside a home-built controlling unit. Similar to the comparison

576 tests at the University of Bern, we have conducted parallel measurements between the CRDS

577 analyzer and the paramagnetic cell at this high altitude site during 03 – 14 February 2017. The

578 measurement of ambient air at the Jungfraujoch system is composed of sequential switching

579 between low span (LS) and high span (HS) calibration gases followed by a target gas (T)

580 measurement (once a day) to evaluate the overall system performance and finally a working

581 gas (WG) measurement before switching back to ambient air.

582 Figure 16 (top panel) shows the calibrated 1-minute averaged O_2 mixing ratios

583 measured at this high altitude site in comparison with the Paramagnetic oxygen analyzer

584 already available at the site. Despite the strong variability observed during the measurement

585 period of 10-days by both analyzers, a very good agreement was observed between them.

586 Figure 16 (bottom panel) shows the absolute difference of 1-minute averages in

587 atmospheric O_2 measured at Jungfraujoch between the two analyzers which are mostly within

588 ±5 ppm range (but sometimes going as high as ±10 ppm) without an offset. However, for

589 generally reported 10-minutes, half-hourly or hourly means these values correspond to < 1.5

590 ppm, < 1 ppm and < 0.65 ppm.

591 3.3.2. Tests at the Beromünster tall tower site

592 The Beromünster tower is located near the southern border of the Swiss Plateau, the

593 comparatively flat part of Switzerland between the Alps in the south and the Jura mountains

594 in the northwest (47° 11′ 23″ N, 8° 10' 32″ E, 797 m a.s.l.), which is characterized by intense

595 agriculture and rather high population density. A detailed description of the tower

596 measurement system as well as a characterization of the site with respect to local

597 meteorological conditions, seasonal and diurnal variations of greenhouse gases, and regional

598 representativeness can be obtained from previous publications (Berhanu et al., 2016; Berhanu

599 et al., 2017; Oney et al., 2015; Satar et al., 2016). The tower is 217.5 m tall with access to five

600 sampling heights (12.5 m, 44.6 m, 71.5 m, 131.6 m, 212.5 m) for measuring CO, CO_2, CH_4

601 and H_2O using Cavity Ring Down Spectroscopy (Picarro Inc., G-2401). By sequentially

602 switching from the highest to the lowest level, mixing ratios of these trace gases were

603 recorded continuously for three minutes per height, but only the last 60 seconds were retained

604 for data analysis. The calibration procedure for ambient air includes measurements of

605 reference gases with high and low mixing ratios traceable to international standards (WMO-

606 X2007 for CO_2 and WMO-X2004 for CO and CH_4), as well as target gas and more frequent

607 working gas determinations to ensure the quality of the measurement system. From two years

608 of data a long-term reproducibility of 2.79 ppb, 0.05 ppm, and 0.29 ppb for CO, CO_2 and

609 CH_4, respectively was determined for this system (Berhanu et al., 2016).

610 Between 15.02.2017 and 02.03.2017, we have connected the new CRDS oxygen

611 analyzer in series with the CO_2 analyzer (Picarro G-2401) and measured the O_2 mixing ratios

612 at the corresponding heights. Similar to the CO_2 measurements, O_2 was also measured for

613 three minutes at each height. During this period, we have evaluated the two features (isotopic

614 mode and concentration mode) of the CRDS analyzer. In the isotopic mode, the CRDS

615 measures the $\delta^{18}O$ values as well as the O_2 concentration while in concentration mode only

616 the latter was measured.

617 During the tests conducted at this tower site, we first evaluated the two operational

618 modes (concentration vs isotopic modes) of the CRDS analyzer. Ambient air measurements

619   on isotopic mode over a 4-days period showed a strong variability in the measured oxygen

620   mixing ratios and it was not possible to distinguish the variability in the O_2 mixing ratios

621   among the five height levels. The calculated 1-minute standard error for ambient air

622   measurements was as high as 10 ppm while a standard error of less than 1 ppm was

623   determined from similar measurements in the concentration mode. Additionally, comparing

624   the O_2 values between the two modes, frequent short time variation in ambient air O_2 (~ 200

625   ppm) was observed in the isotope mode measurements while the variation in the concentration

626   mode is significantly smaller (~ 30 ppm). This precision degradation is due to the weaker ^{16}O

627   oxygen line used for the isotopic mode, and the fact that far more ring-downs are collected on

628   the rare isotopologue in isotopic mode Hence, we have conducted the remaining test

629   measurements in concentration mode.

630   As this tower has five sampling height levels, we first followed three minutes of

631   switching per inlet level, which enables four measurements per hour at a given level.

632   However, we noticed hardly any difference among the different levels due to strong short

633   term variability in O_2 mixing ratios between the consecutive heights. Hence, we switched to a

634   longer sampling period of six-minutes per height. Figure 17 shows the diurnal CO_2 and O_2

635   variations at the lowest (12 m) and highest (212.5 m) sampling heights of the tower. These

636   two heights were selected simply to better illustrate the difference in the mixing ratios. The

637   CO_2 mixing ratios on the top panel show higher values at the 12 m inlet than the highest level

638   most of the day due to its closeness to sources except during the afternoon (11:00 - 17:00

639   UTC) when both levels show similar but decreasing CO_2 mixing ratios. This is due to

640   presence of a well-mixed planetary boundary layer (PBL) (Satar et al., 2016). The lag in CO_2

641   peak between the two height levels by about two hours indicates the duration for uniform

642   vertical mixing along the tower during winter 2017. The opposite variability patterns are also

643   clearly visible in the O_2 mixing ratios shown in the lower panel with a clear distinction

644   between the two height levels during early in the morning and in the evening while similar O_2

645   values were observed in the afternoon. These opposing profiles are expected as CO_2 and O_2

646   are linearly coupled with a mean oxidation ratio of -1.1 ± 0.05 (Severinghaus, 1995) for land-

647   biospheric processes (photosynthesis and respiration) and -1.44 ± 0.03 for fossil fuel burning

648   (Keeling, 1988b).

649   Table 2 shows the oxidation ratios derived as the slopes of the linear regression

650   between CO_2 and O_2 mixing ratios at the different height levels measured on 25 February

651   2017. Accordingly, height dependent slopes were observed with a slope of -0.98 ± 0.06 at the

652   lowest level, close to the biological processes induced slope but slightly lower than its mean

653   value. For the highest level, we calculated a slope of -1.60 ± 0.07 a value close to fossil fuel

654   combustion oxidation ratio. Note that depending on fossil fuel type the oxidation ratio can

655   range between -1.17 and -1.95 for coal and natural gas, respectively (Keeling, 1988b). While

656   the slopes derived for the two other levels (44.6 m and 131.6 m) show similar values between

657   the highest and lowest height levels, possibly from mixed sources, the middle level showed a

658   slightly higher slope than these two levels but still in the large range between the lowest and

659   highest inlet heights.

660   3.4. Evaluation of the $\delta^{18}O$ measurements

661   To further evaluate the analyzer's performance in measuring stable oxygen isotopes,

662   we conducted ambient air isotopic composition measurements as well as analyzed a standard

663   gas without CO_2 which has a known $\delta^{18}O$ value. The choice of this CO_2-free air standard gas

664   is twofold: one it has a known $\delta^{18}O$ value and second as it has no interference from possible

665   CO_2 absorption band overlap. For this test three 0.5 L glass flasks were preconditioned and

666   filled with this standard gas to ambient pressure. These flasks were attached before or after

667 the water trap (Fig. 11) and measured similar to ambient air measurements. These

668 measurements were then compared with $\delta(^{34}O/^{32}O)$ values obtained by parallel measurements

669 using our IRMS.

670   Figure 18 shows the $\delta^{18}O$ values of ambient air from the roof top with three

671 consecutive measurements of glass flasks filled with CO_2-free air in-between followed by a

672 fourth flask filled with breath air. An excellent agreement was observed for measurements

673 from both instruments for the three flasks filled with a standard gas. However, the fourth flask

674 with breath air showed a signal opposite to the measurements by the IRMS. As breath air

675 contains large amount of water and CO_2 in addition to O_2, which can possibly interfere with

676 the CRDS analyzer measurements, we have removed H_2O and CO_2 by using a cryogenic trap

677 (-130 °C) and in an additional experiment using Schütze reagent to remove both CO and CO_2.

678 However, we have not observed any improvement towards an agreement with the IRMS

679 measurements. Therefore, any other gas component in the breath air must be relevant for the

680 interference. Based on the absorption lines in the spectral range of the instrument (7878 cm^{-1})

681 retrieved from HITRAN database, we expect interference either from carbon monoxide (now

682 excluded by the tests) or methane or VOCs including acetone, ethanol, methanol or isoprenes,

683 all of which have been measured in breath air (Gao et al., 2017; Gottlieb et al., 2017; Mckay

684 et al., 1985; Ryter and Choi, 2013; Wolf et al., 2017). Further investigations have to shed light

685 on these interferences in order to take corresponding action to surpass these shortcomings in

686 the isotope analysis based on cavity ring-down spectroscopy.

687 **4. Conclusions**

688   We have thoroughly evaluated the performance of a new CRDS analyzer which

689 measures O_2 mixing ratios and isotopic composition combining laboratory and field tests.

690 Even if a drift in the analyzer was observed at the beginning of this study, which can be easily

691 corrected by calibration, the recent analyzers built by the manufacturer did not show such

692 instrumental drift. However, prior tests are recommended to see the analyzer's stability.

693 The T-split tests for the current measurement setup based on the measurements of two

694 standard gases showed a difference within the measurement uncertainty. However, this effect

695 may become significant while applying larger splitting ratios and we recommend conducting

696 further experiments to accurately quantify this influence for larger splitting ratios.

697 We have observed a strong influence of dilution in the measured O_2 values during the

698 presence of high CO_2 mixing ratios. Even if such an influence may not be critical for the

699 present study, such an effect might be significant in other studies where higher CO_2 mixing

700 ratios might be present and we recommend following a correction strategy based on parallel

701 CO_2 measurements. This also applies for more accurate analysis.

702 The water correction applied by the instrument's in-built function seems to sufficiently

703 correct for the water vapor influence. However, a larger variability of the difference was

704 observed between the CRDS analyzer and the Paramagnetic cell when dried samples were

705 used in both systems. This can possibly be due to an overcorrection by the water correction

706 function of the CRDS analyzer when dried samples were used. This is particularly true for the

707 very low water vapor range (< 100 ppm). We believe that it is important to further investigate

708 this issue and identify an improved water correction strategy.

709 Based on the analysis of O_2 mixing ratios in the concentration and isotopic modes, we

710 have observed a significant decrease in precision (about ten-fold) in the latter measurement

711 mode. The measured $\delta^{18}O$ values for the standard air by the CRDS analyzer are in excellent

712 agreement with the IRMS values. However, such measurements for a breath air showed a

713 contrasting signal, possibly due to interference from other gases such as CH_4. Hence, we

714 recommend further investigation on such possible contaminants and how to possibly remove

them while conducting ambient air measurements. However, we believe that this analyzer can be used for tracer experiments where artificially enriched isotopes are used to study biological processes such as photosynthesis in plants using isotopically labelled CO_2 and H_2O.

Acknowledgement

We would like to thank ICOS-RI and the Swiss National Science Foundation (SNF) for funding ICOS-CH (20FI21_148994, 20FI21_148992). We are also grateful to the International Foundation High Alpine Research Stations Jungfraujoch and Gornergrat. The measurement system at the Beromünster tower was built and maintained by the CarboCount-CH (CRSII2_136273) and IsoCEP (200020_172550) projects both funded by SNF.

List of Tables

Table 1. Assigned mixing ratios of standard gases used in this study and their corresponding values measured by the NDIR, CRDS and IRMS at the University of Bern. [1]The assigned values are based on measurements from different institutions (University of Bern (UB),

739 Scripps or NOAA, see column cylinder name). [2]Measurements are on the Bern scale for CO_2

740 and O_2. The Bern scale is shifted by +550 per meg. [3]Values on the Scripps scale.

741

Cylinder name	Assigned CO_2 (ppm) [1]	Assigned O_2 (per meg) [1]	CO_2-IRMS (ppm) [2]	CO_2-NDIR (ppm) [2]	O_2-IRMS (per meg) [2]	O_2-Paramagnetic (per meg) [2]	O_2-CRDS (per meg) [2]
ST-1 LUX3576-UB	427.47	-1026	427.47	427.59	-1026	-1070	-1057
ST-2 LK922131-UB	368.09	599	368.09	367.82	599	560	590
ST-3 CA07045-Scripps	382.303	-271.6	382.50	381.99	278 (-272.2)[3]	302	281
ST-4 CA07043-Scripps	390.528	-476.4	390.69	390.15	71 (-479.5)[3]	66	63
ST-5 CA07047-Scripps	374.480	-807.7	374.70	374.17	-253 (-803.3)[3]	-212	-233
ST-6 CA04556-NOAA	192.44	-3410	191.21	191.64	-3410	-2905	-3013
ST-7 CA06943-NOAA	2699.45	-		2612.80	-	-2691	-3369
ST-8 LK76852-UB	411.49	37794	411.49	406.25	37794	34513	36017

742

743

Table 2. The CO_2 and O_2 correlation coefficients at the different height levels derived using the least square fit and the correlation coefficients (r^2). Uncertainties are calculated as standard error of the slope.

Height	Oxidation Ratios (O_2:CO_2)
12.5 m	-0.98 ± 0.06 (0.48)
44.6 m	-1.29 ± 0.07 (0.50)
71.5 m	-1.49 ± 0.08 (0.47)
131.6 m	-1.23 ± 0.05 (0.55)
212.5 m	-1.60 ± 0.07 (0.61)

747

748

749

750

751

752

753

754

755   List of Figures
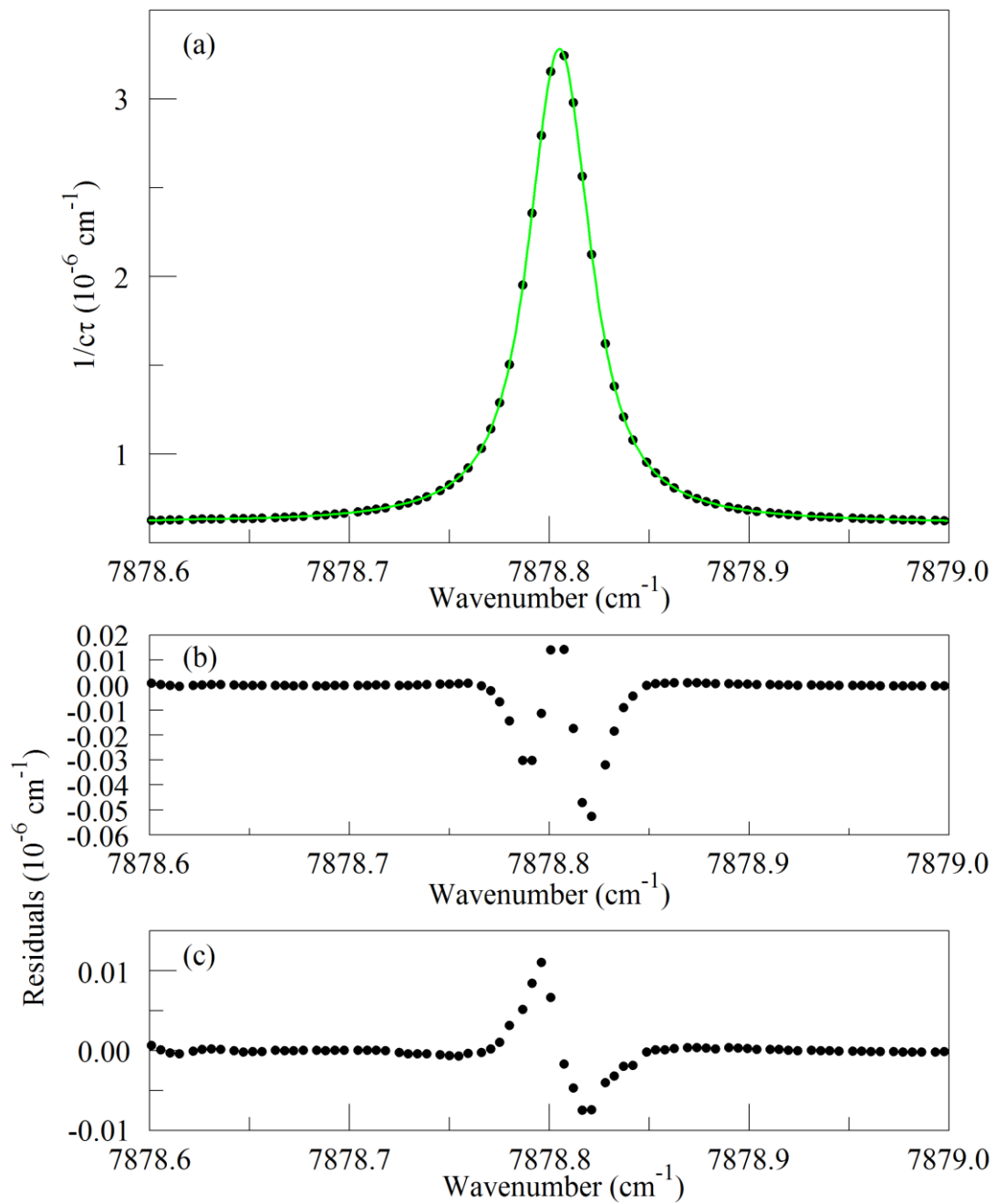
Figure 1. The top panel (a) shows the raw data (points) and the best-fit Galatry function (solid line). Residuals of the Voigt fit are shown in panel (b) and residuals of the Galatry fit are shown in panel (c).
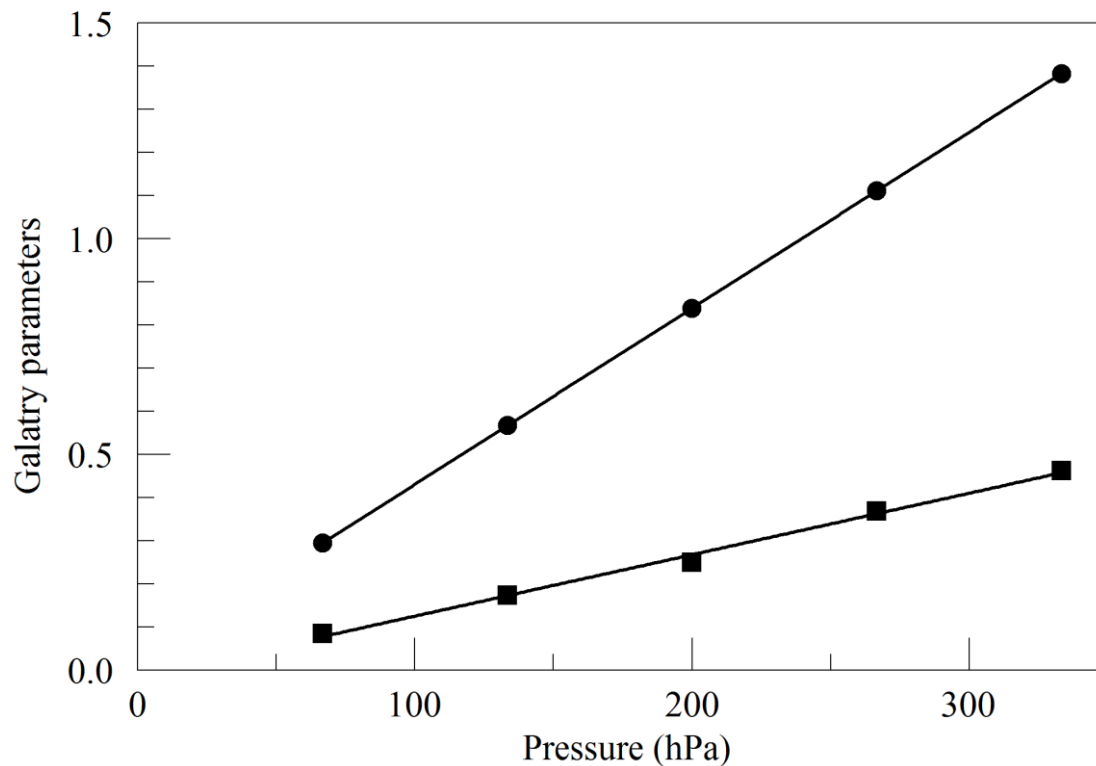
762

763   Figure 2. Best-fit values for the Galatry parameters of the Q13Q13 line of O_2, as a function of

764   pressure. The line broadening parameter y is represented by circles and the line narrowing

765   parameter z by squares. The solid lines are linear fits to the measurements. The best-fit offset

766   and slope are 0.0227 and 0.004082 hPa^{-1} for y, and -0.0169 and 0.001424 hPa^{-1} for z.
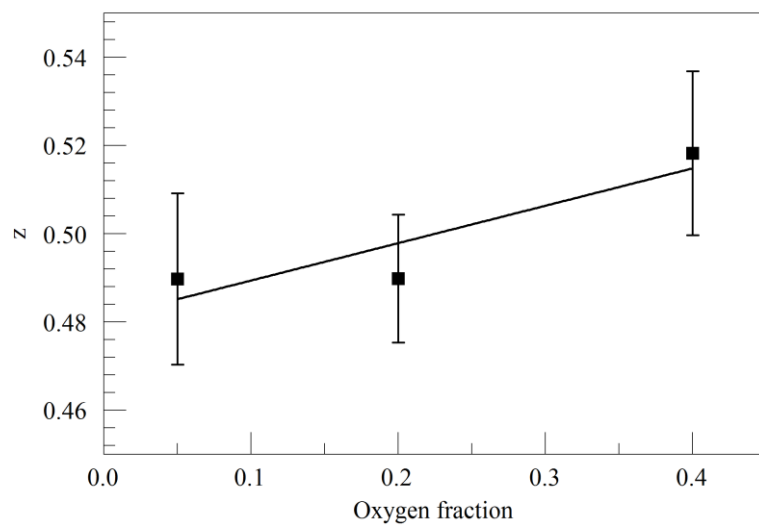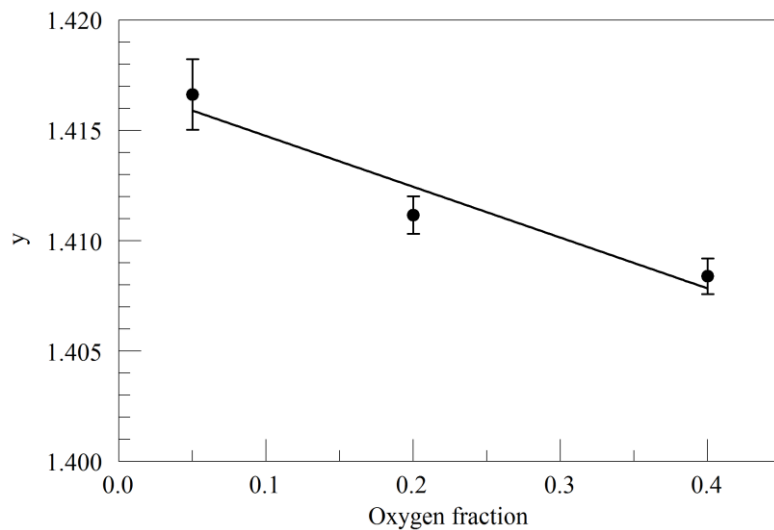
767

768   Figure 3. Galatry parameters of the Q13Q13 line of O_2 at 340 hPa and 45° C as a function of

769   O_2 mole fraction in binary O_2 - N_2 mixtures. The linear fits to the data are y = 1.417 – 0.023 x

770   f_{O2} and z = 0.481 + 0.085 x f_{O2}.
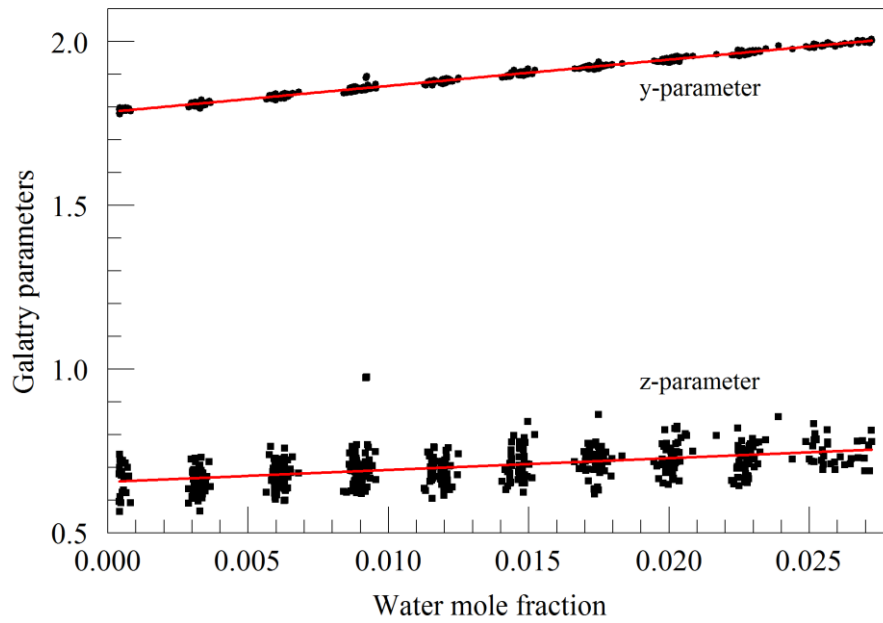
771

772 Figure 4. Galatry parameters of the 7816.75210 cm^{-1} water line in air at 340 hPa and 45° C as

773 a function of water mole fraction. Black points are from measurements and red lines are

774 linear fits: $y = 1.7846 + 8.01 \times f_{H2O}$ and $z = 0.656 + 3.60 \times f_{H2O}$.

775

776

777
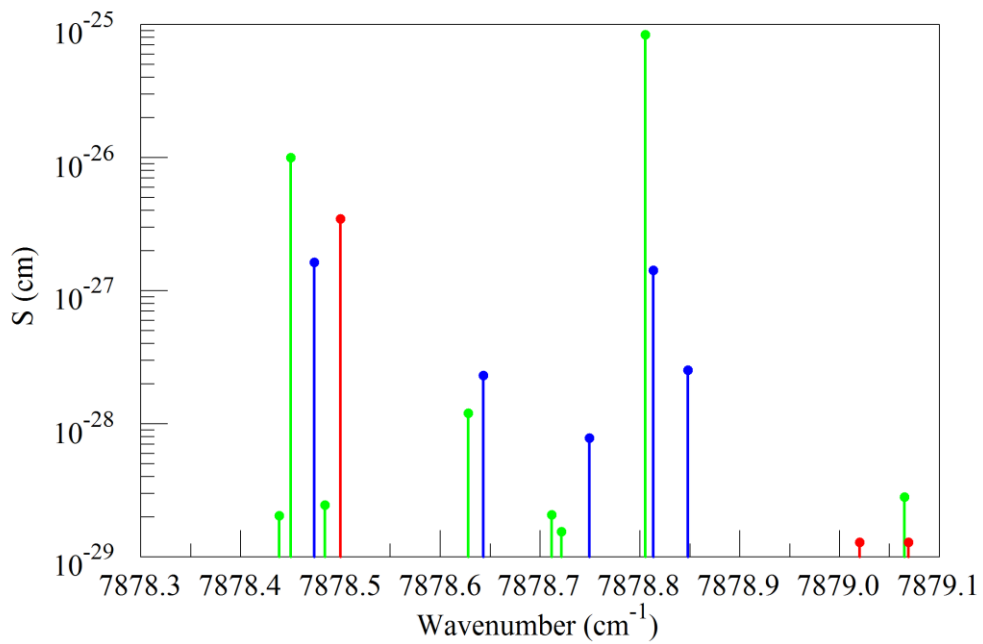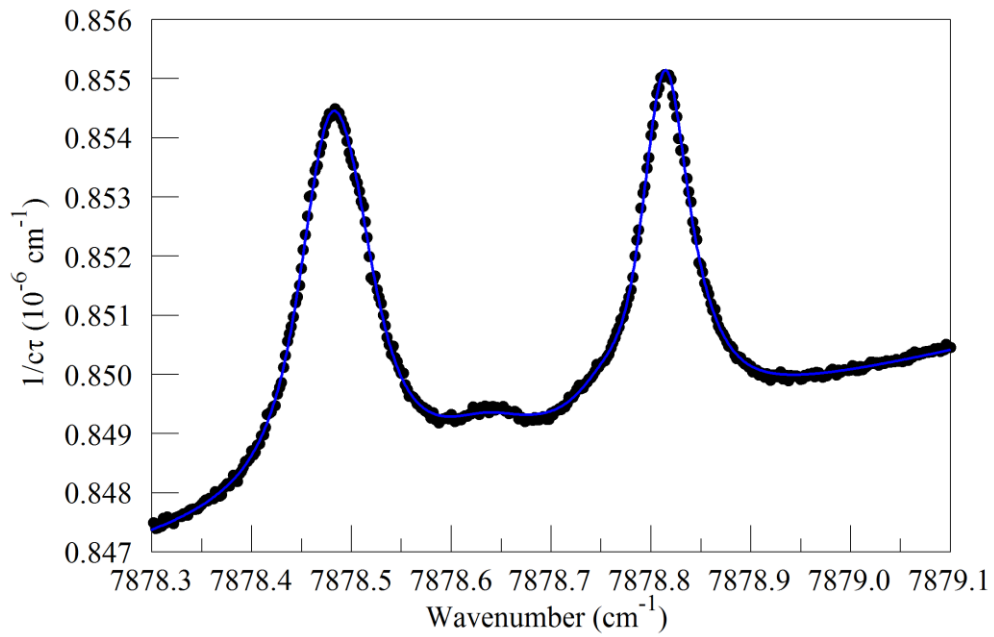
778

779 Figure 5. Upper panel: spectrum of water in nitrogen (points) and fit to Voigt model (blue

780 curve). Lower panel: Oxygen (green), normal water (blue), and deuterated water (red) lines

781 in the 2016 Hitran data base.

782

783
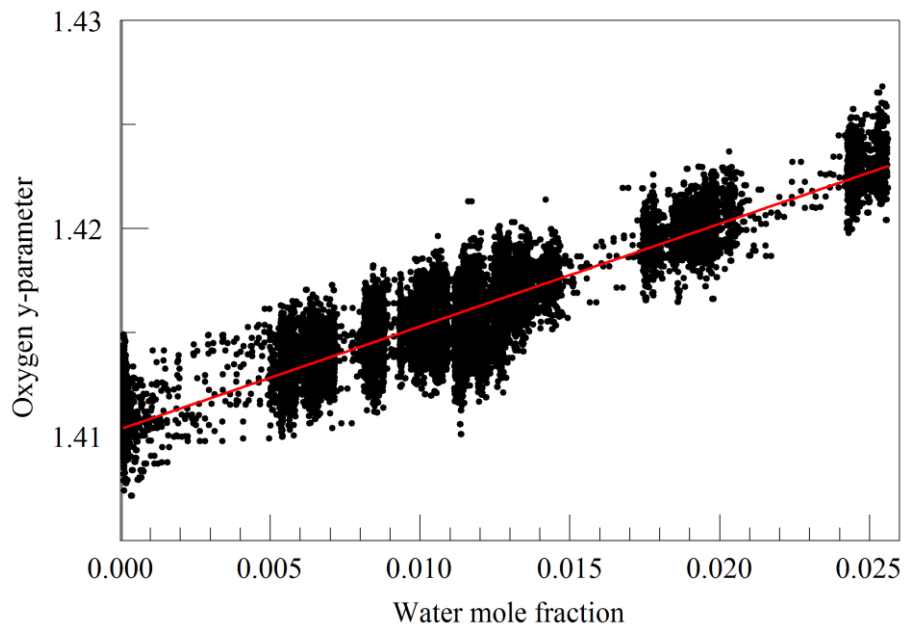
784

785   Figure 6.   Galatry collisional broadening parameter of the oxygen Q13Q13 line at 340 hPa

786   and 45° C versus water mole fraction. Black points are from measurements and the red line is

787   a linear fit: $y = 1.4109 + 0.467\ f_{H2O}$.

788

789

790
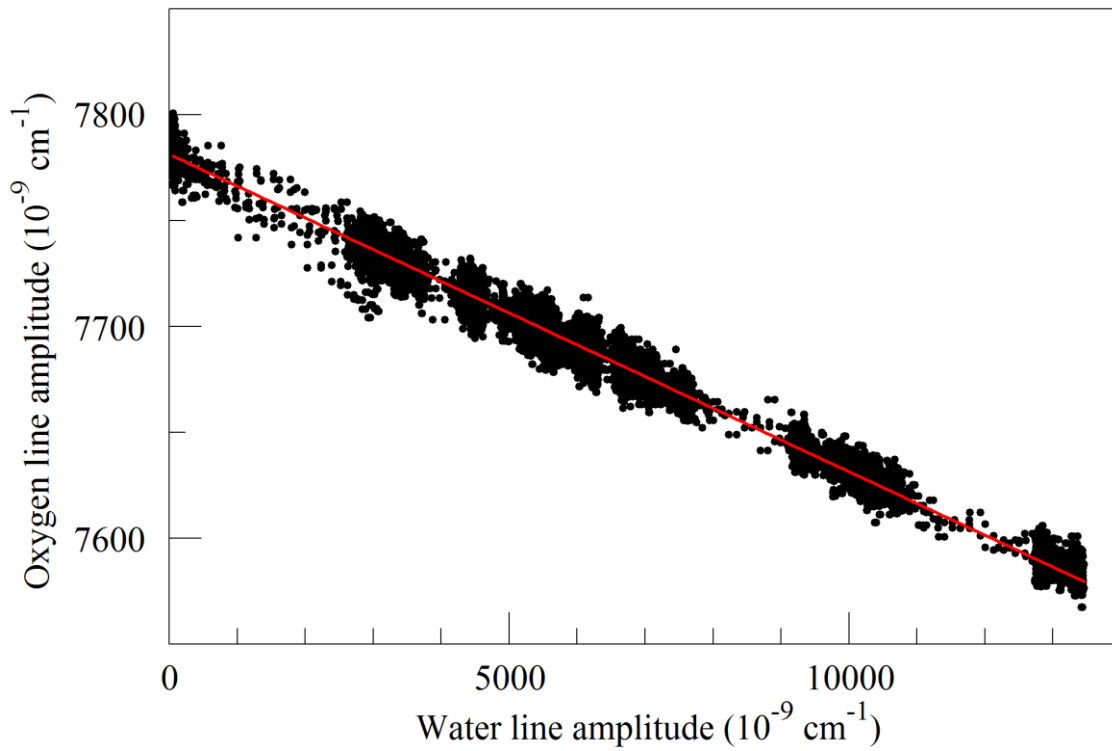
791

792 Figure 7. Measured absorption line amplitudes for oxygen and water vapor for water vapor

793 mixing ratios ranging from nearly 0 to 0.025. Black points are from measurements and the

794 red line is a linear fit: with intercept 7.78001×10^{-6} cm^{-1} and slope -0.014807.

795

796

797

798

799

800
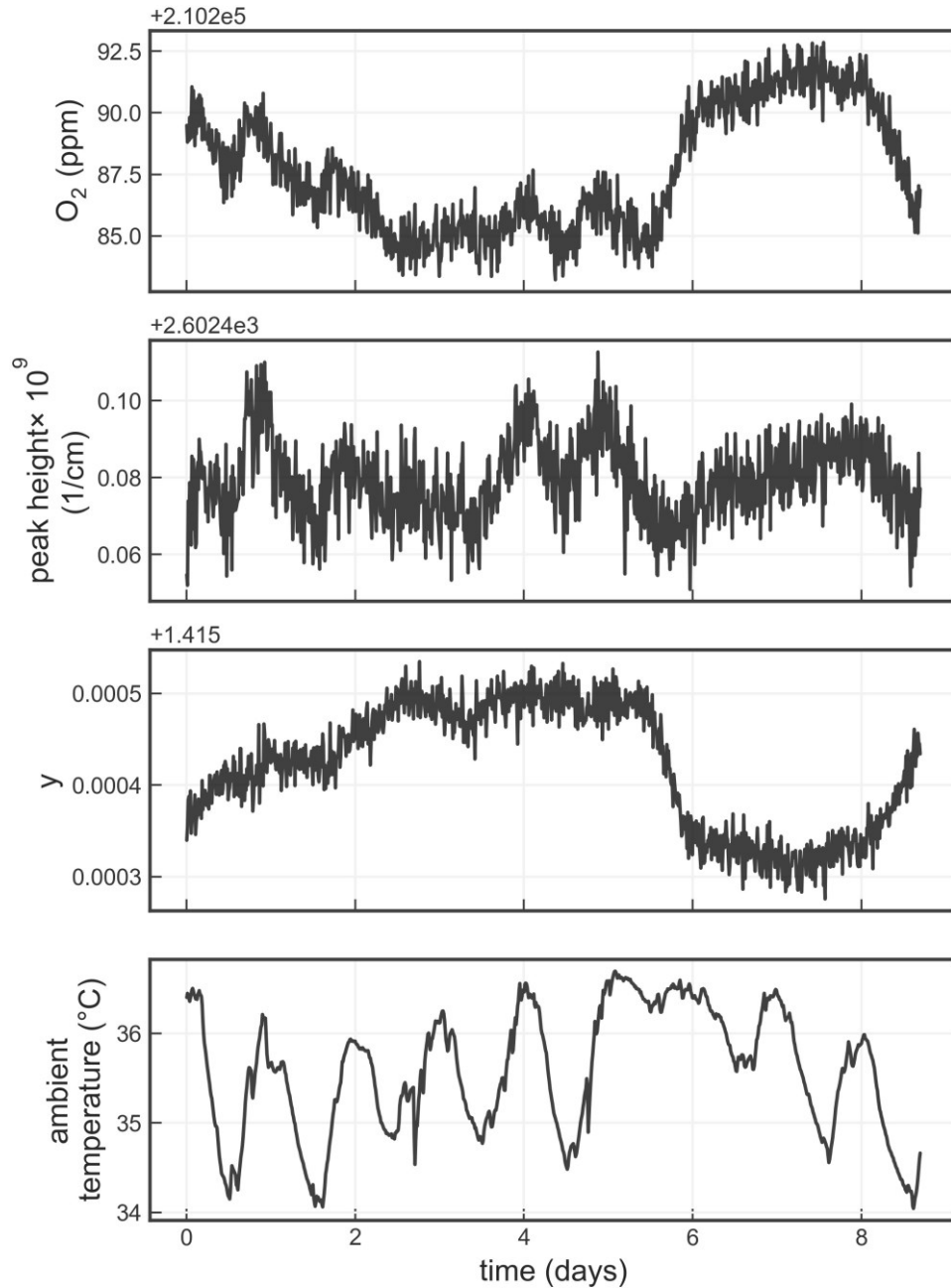
801

802 Figure 8. Time series from a measurement of a single tank over about a week. The four panels

803 show the water-corrected oxygen concentration, the absorption peak loss minus the baseline

804 loss, the measured Lorentzian broadening factor, and the ambient temperature (measured in

805 the instrument housing), respectively. A windowed average of 300 seconds was applied to all

806 four data sets.
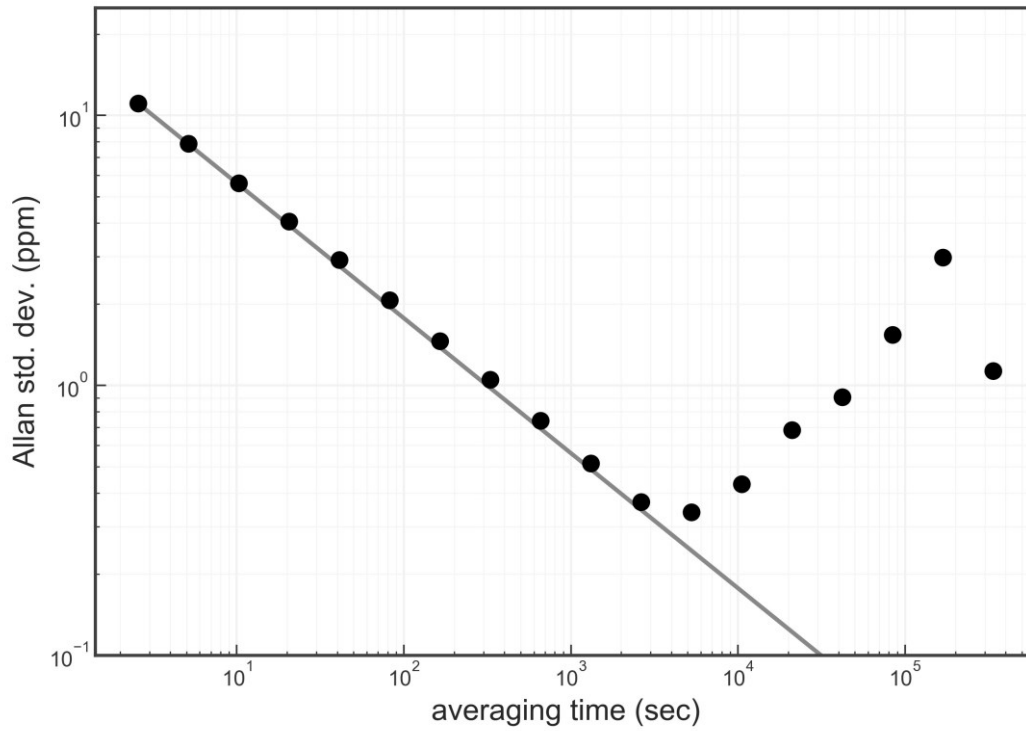
807

808   Figure 9. Precision of O_2 mole fraction measured from a tank of synthetic air. Filled circles

809   are measurements and the line shows the ideal $\tau^{-1/2}$ dependence.

810

811

812

813

814
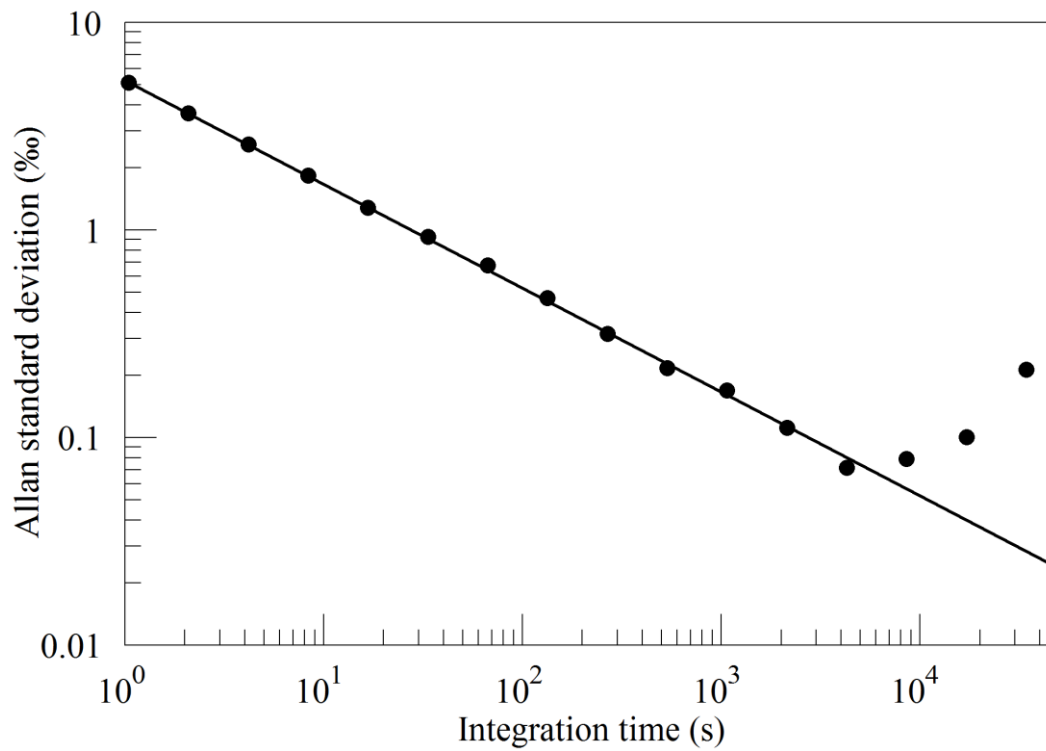
Figure 10. Precision of $\delta(^{18}O)$ measured from a tank of synthetic air. Filled circles are

measurements and the line shows the ideal $\tau^{-1/2}$ dependence.
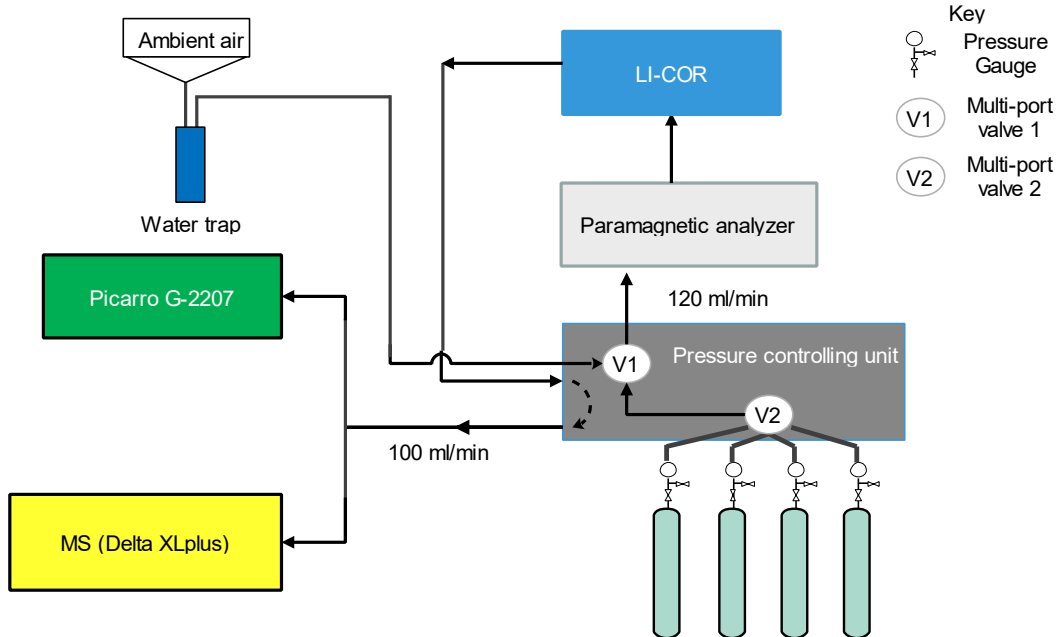
826

827 Figure 11. Schematics of the measurement system used to compare the Picarro analyzer with

828 the Mass Spectrometer at Bern.

829

830

831

832

833

834

835

836

837
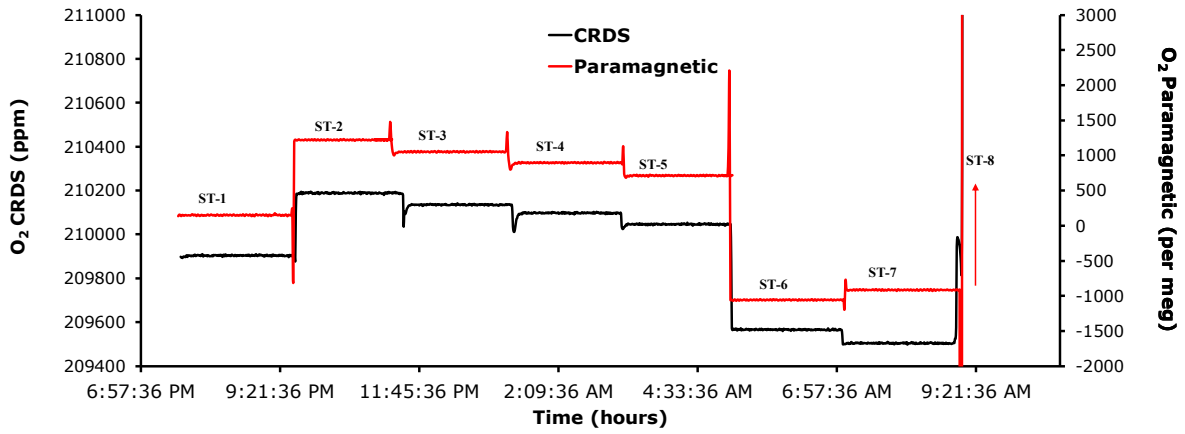
838

839 Figure 12. Comparison of oxygen mixing ratios for the seven standard gases measured using

840 the CRDS analyzer (black) and the Paramagnetic sensors (red).

841

842

843

844

845

846

847

848

849

850

851

852

853

854

855

856

857
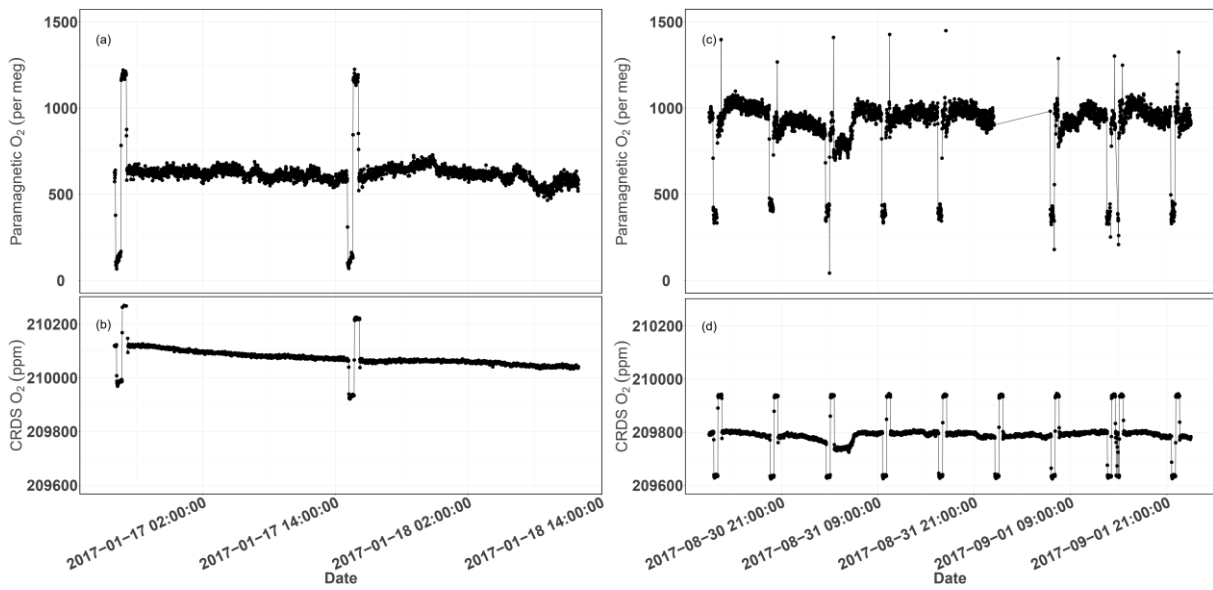
Figure 13. Parallel ambient air measurements by the Paramagnetic and CRDS analyzers at the

beginning of the testing period (Panels a & b, January 2017) and the second phase of testing

(Panels c & d, September 2017). The spikes are measurements from the two standard gases

bracketing the ambient air values.

862

863

864

865

866

867

868

869

870

871

872

873
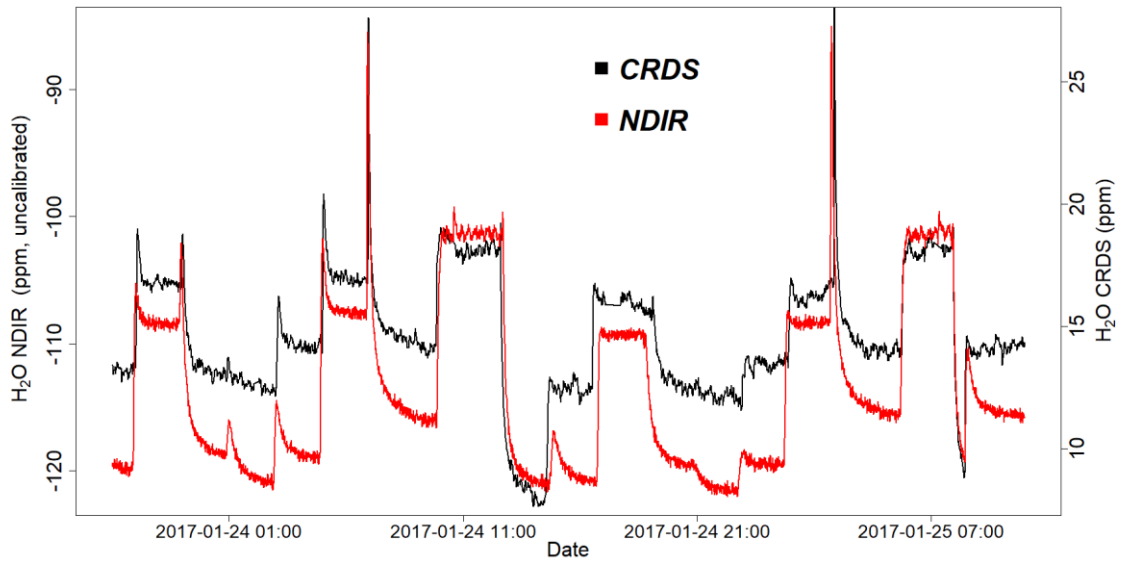
874

875   Figure 14. Parallel water vapor measurements for a dried ambient air by both the NDIR and

876   CRDS analyzers. Note that the water values from the NDIR analyzer are not calibrated.

877

878

879

880

881

882

883

884

885

886

887

888

889

890

891
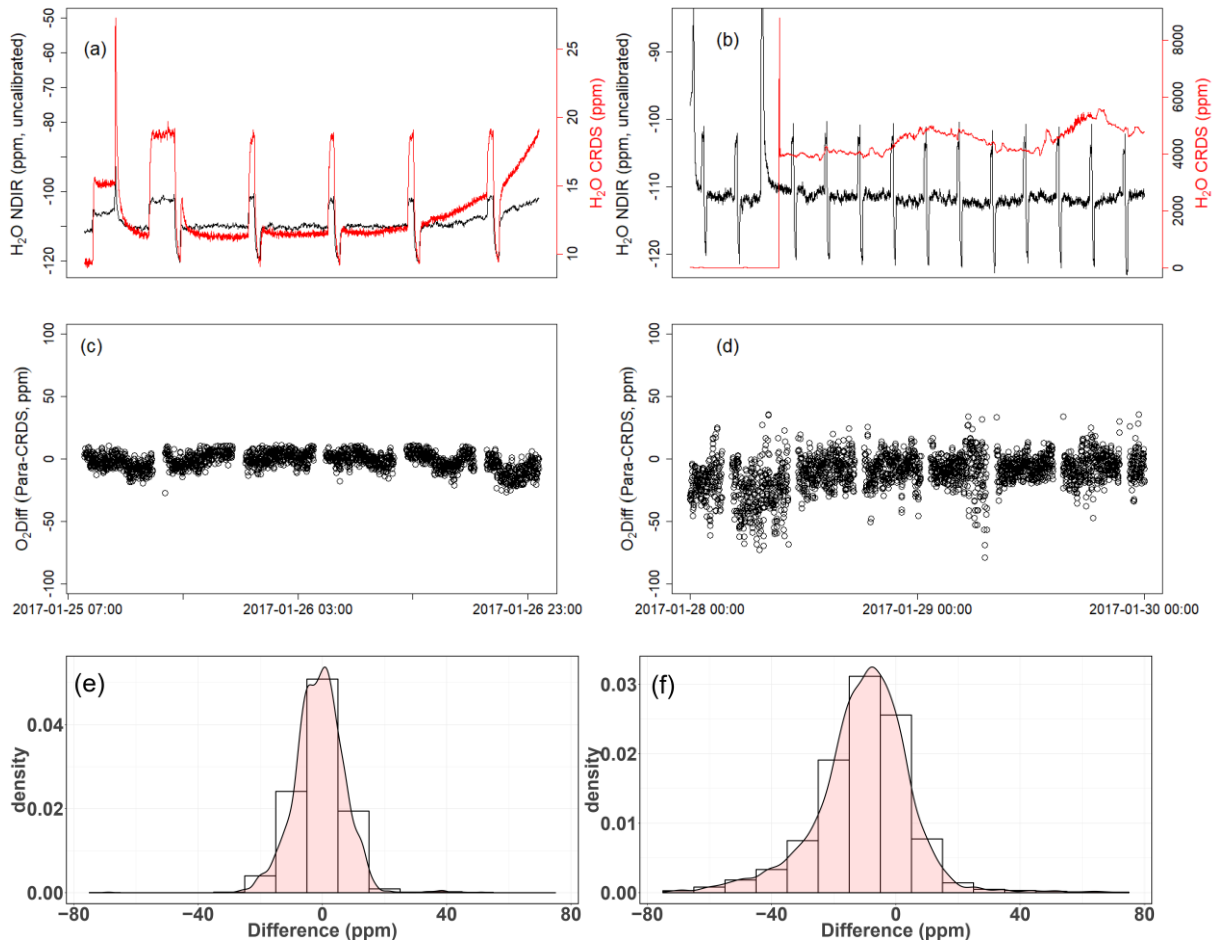
Figure 15. Results of water correction tests. Water measurements of the NDIR (left scale) for

dry conditions (a,b) and the CRDS analyzer (right scale) for dry (a) and wet (b) conditions.

The difference in oxygen measurements between the Paramagnetic and the CRDS instrument

using the built-in water correction for the CRDS values under dry (c) and wet (d) conditions.

Panels (e) and (f) show the population density functions.

897

898

899

900

901
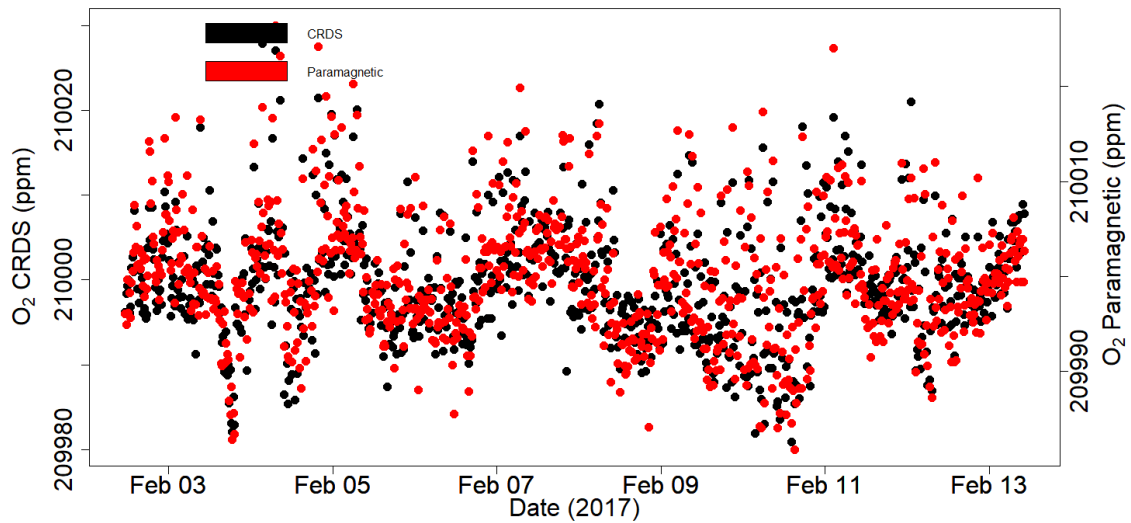
902
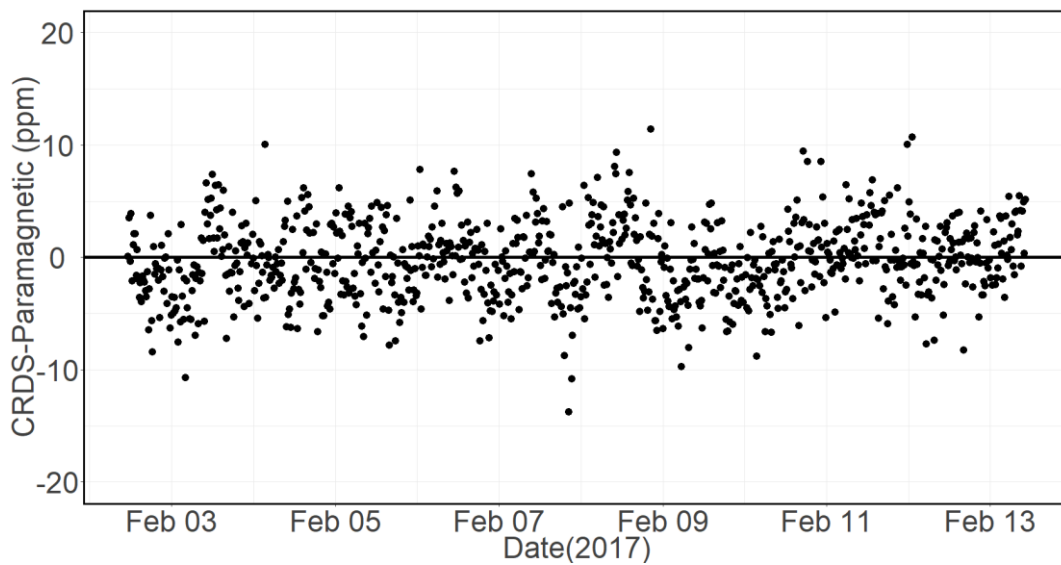
903

904 Figure 16. Calibrated ambient air oxygen measurements (1-minute average) at the

905 Jungfraujoch site using the CRDS and Paramagnetic analyzers both in ppm units (a) and the

906 absolute difference between the two measurements in ppm (b) by matching time stamps

907

908

909

910

911

912
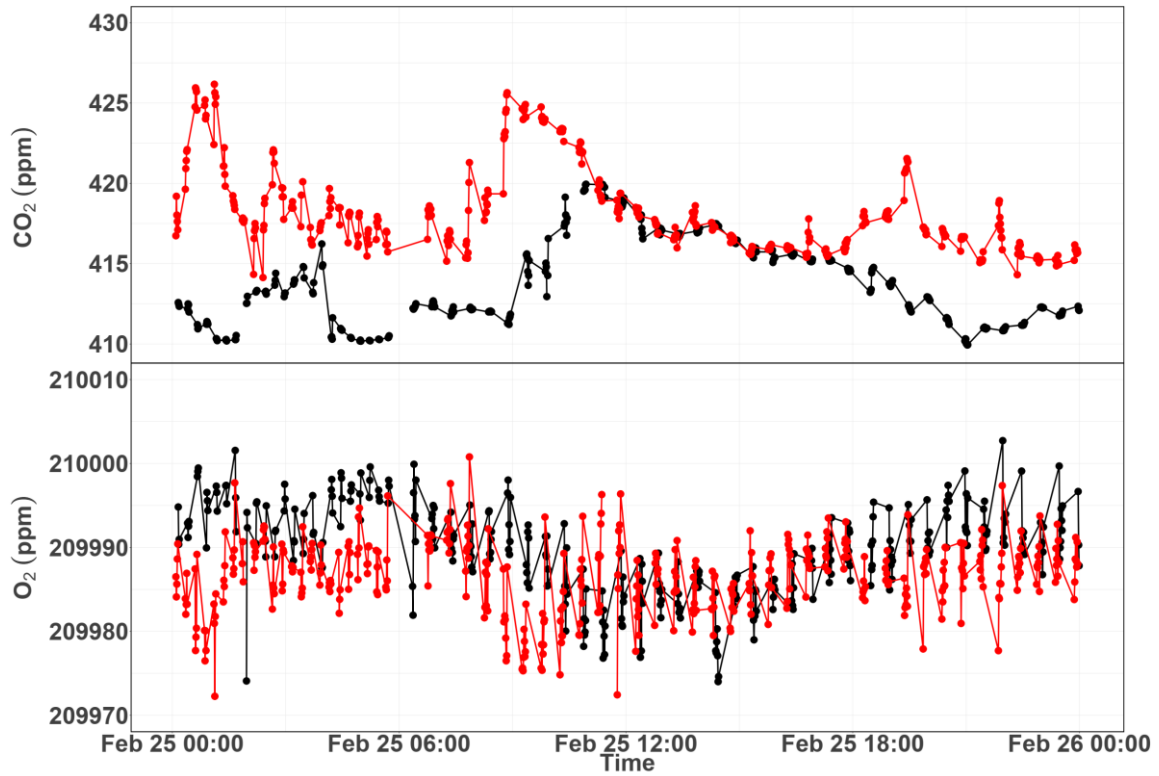
Figure 17. Diurnal variations of CO_2 (top) and O_2 (bottom) measurements from the 12 m (red)

and the 212.5 m (black) height levels at Beromünster tower.

915

916

917

918

919

920

921

922

923

924
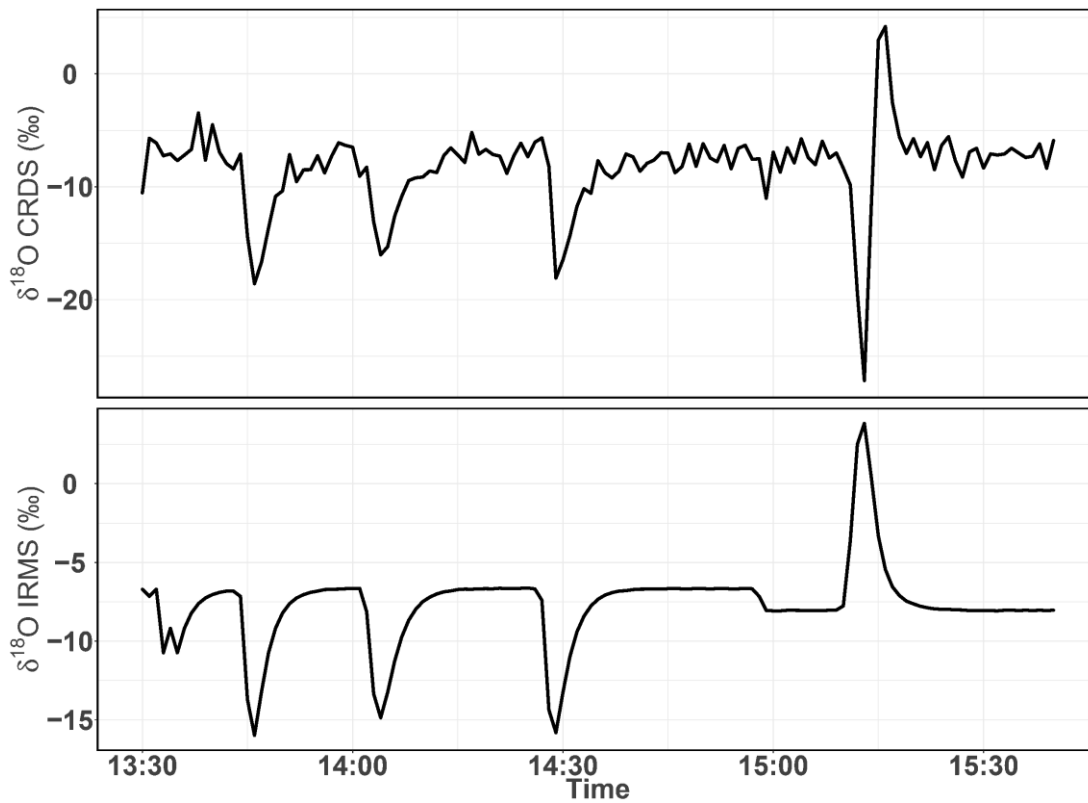
Figure 18. Consecutive $\delta^{18}O$ measurements of a standard gas (CO_2-free air) filled into three flasks followed by measurement of breath air using the CRDS analyzer (top) and IRMS (bottom). These measurements were carried out in the middle of ambient air measurements.

Appendix A.
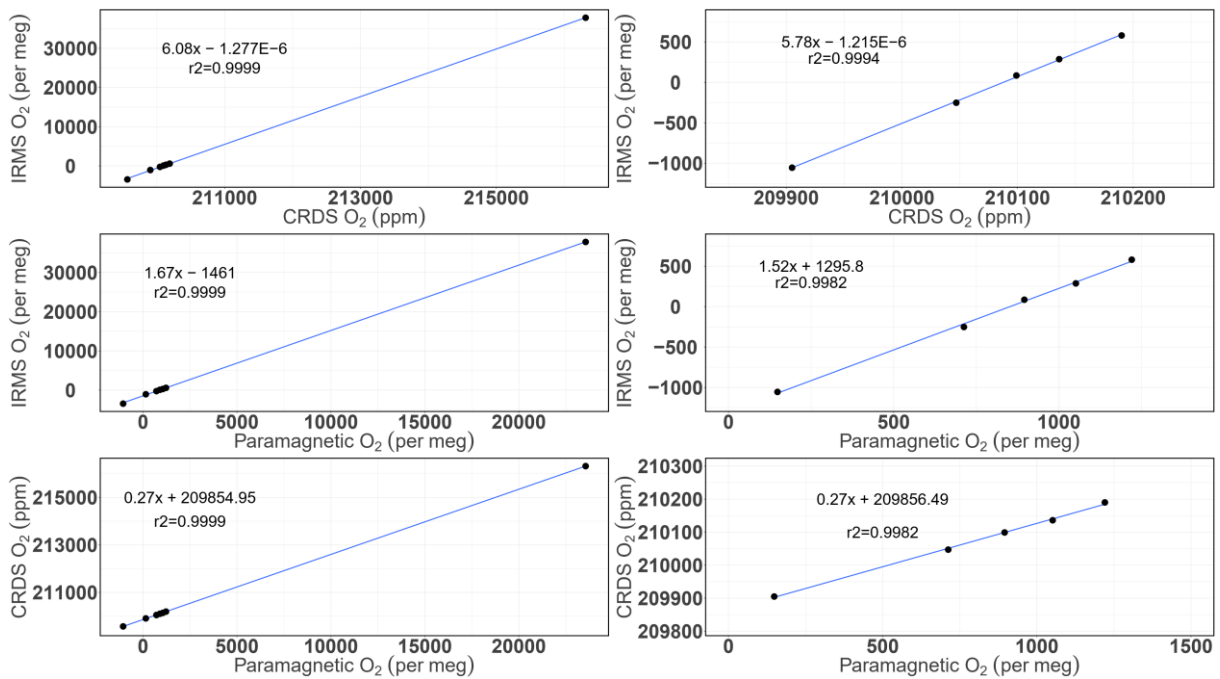
Figure A.1. Correlations between the O_2 mixing ratios measured by the CRDS and Paramagnetic analyzers with the mass spectrometric measurements (uncalibrated values). The left panels are for all the cylinders measured (standards 1 to 8) while the right ones are after selecting standards 1-5.

Appendix B: Uncertainty consideration during conversion of ppm to per meg

954

955 Generally, the Delta notation ($\delta(O_2/N_2)$), as given in equation 1 of this publication (also

956 shown below), is used in order to circumvent the influences of dilution by other gas

957 components when determining oxygen mole fractions. Yet, several instruments are measuring

958 the oxygen mole fraction such as the paramagnetic cell, the UV-cell as well as the instrument

959 by CRDS analyzer presented here. Therefore, a thorough consideration of the conversion

960 from ppm (mole fraction) to per meg ($\delta(O_2/N_2)$ notation) is necessary which is explained in

961 this appendix.

962 Following equation 1 in Thojima et al., 2000, the per meg to ppm conversion has a slope of

963 6.04 if only a change in oxygen is applied as seen in table A1. It changes slightly to 6.11 per

964 meg per ppm, when we talk about nitrogen changes only, or to a slope zero (horizontal line)

965 when talking about any other changes of air components excluding oxygen and nitrogen. The

966 fact that our supplementary plot shows slopes of 5.78 (for the first five standards) or 6.08 (for

967 all standards except ST-7) is due to a mixed influence dilution effects. The lower slope of

968 5.78 documents particularly the influence of the CO_2 dilution effect.

$$\delta\left(\frac{O_2}{N_2}\right)(per\ meg) = \left(\frac{\left(\frac{O_2}{N_2}\right)_{sample}}{\left(\frac{O_2}{N_2}\right)_{reference}} - 1\right).10^6 \qquad (1)$$

969

970 Note that under the assumption the atmospheric N_2 content is constant (i.e. $N_{2sample}$ equals

971 $N_{2reference}$), we convert relative changes in oxygen given in per meg following equation 1 to

972 oxygen changes in parts per million (equivalent to micromol/mol) by multiplying by the O_2

973 mole fraction ($O_{2reference}$) expressed as 209500 ppm (the O_2 mole fraction of atmospheric air)

974 (Machta and Hughes, 1970). Hence 1 ppm corresponds approximately to 4.8 per meg, or 1 per

975 meg to 1/4.8 (209500/106) ppm.

976   This is used in our approach since the Picarro instrument measures the O_2 concentration

977   which requires to be converted to an O_2/N_2 ratio. Since no information about N_2 is available

978   one assumes a constant value, i.e. N_2 of the standard. Therefore, eq. 1 in the manuscript

979   reduces to $(O_{2,SA}/O_{2,ST}-1)$ *x* 10^6 or $\Delta O_2/O_{2,ST}$ *x* 10^6. The value obtained is an estimated

980     $\delta O_2/N_{2,est}$ ratio, which indeed is slightly different from the true $\delta O_2/N_{2,true}$. The effect of water

981   dilution (amount of water vapor is measured by the CRDS instrument) is taken into account as

982   described in the manuscript. Yet any other dilution effect is not considered except if

983   additional information is available, e.g. CO_2 concentration measurements. Indeed this dilution

984   effects can be significant and are displayed in the following table A1.

985   Table A1: ppm to per meg conversion calculations for air-like compositions

Change in ppm		ΔO_2 apparent (change + dilution effect)	$\delta O_2/N_{2,true}$ (per meg) ($\delta O_2/N_{2,true}/\Delta O_2$ in per meg/ppm)		$\delta O_2/N_{2,est}$ (per meg) ($\delta O_2/O_{2,est}/\Delta O_2$ in per meg/ppm)		Difference in $\delta O_2/N_2$ (true – est) in per meg
ΔCO_2 only	10	-2.0946	0	(0)	-10	(4.77)	10
ΔAr only	10	-2.0946	0	(0)	-10	(4.77)	10
ΔO_2 only	10	7.9054	47.74	(6.04)	37.74	(4.77)	10
ΔO_2 only	10	-2.0946	-12.81	(6.11)	-10	(4.77)	-2.81

986

987     $\delta O_2/N_{2,true}$: for instance measured by mass spectrometry; $\delta O_2/N_{2,est}$: for instance measured by

988   Picarro G-2207.

989   Incorrectly assumed N_2, Ar, CO_2 or any additional gas component can lead to changes in the

990   estimated $\delta O_2/N_{2,est}$ values as stated in the table A1. For example a 10 ppm increase in CO_2

991   lead to an incorrect value of -10 per meg in $\delta O_2/N_{2,est}$ compared to the true $\delta O_2/N_{2,true}$ value.

992   This is simply the dilution effect that the increased CO_2 concentration has on the

993   corresponding O_2 concentration measurements (dilution in oxygen corresponds to the

994   percentage-wise assignment of the excess CO_2 in ppm to oxygen, i.e. -10 ppm x oxygen mole

995   fraction = 2.0946, if O_2 mole fraction corresponds to 0.20946). As you can see from table A1

996   an addition of N_2 of 10 ppm leads to a reduced and opposite effect for the difference in

997    $\delta O_2/N_2$ (true – est) because the dilution effect on O_2 cannot compensate the change from the

998   increase in nitrogen, therefore it scales with -10 ppm x (oxygen mole fraction/nitrogen mole

999   fraction). This also shows that the difference in the Delta values (true – est) scales with the

1000 $\delta O_2/N_2$ ratio present in the sample. Therefore, best results are obtained when the calibration

1001   gases for which the gas composition is known equals closely the sample gas composition. In

1002   our case this is given – but can certainly be improved – since we are comparing air

1003   composition to air standard compositions. Yet, determinations of the standards that has been

1004   used in this study have a range in N_2 concentrations of -110 to +110 ppm for the ST-1 to ST-

1005   5, whereas ST-6 (+700 ppm) and ST-8 (-6200 ppm) are significantly off compared to our

1006   primary standard used for mass spectrometric determination. Therefore, special attention is

1007   required for the precise determination of standard gas composition and the control of the air

1008   sample composition by means of flask measurements in order to detect potential fractionation

1009   effects during air intake.

1010

1011

1012

1013

1014

1015

References

Battle, M., Bender, M. L., Tans, P. P., White, J. W. C., Ellis, J. T., Conway, T., and Francey, R. J.: Global carbon sinks and their variability inferred from atmospheric O-2 and delta C-13, Science, 287, 2467-2470, 2000.

Bender, M. L., Tans, P. P., Ellis, J. T., Orchardo, J., and Habfast, K.: A High-Precision Isotope Ratio Mass-Spectrometry Method for Measuring the O-2 N-2 Ratio of Air, Geochim Cosmochim Ac, 58, 4751-4758, 1994.

Berhanu, T. A., Satar, E., Schanda, R., Nyfeler, P., Moret, H., Brunner, D., Oney, B., and Leuenberger, M.: Measurements of greenhouse gases at Beromünster tall tower station in Switzerland, Atmos. Meas. Tech. , 9, 2016.

Berhanu, T. A., Szidat, S., Brunner, D., Satar, E., Schanda, R., Nyfeler, P., Battaglia, M., Steinbacher, M., Hammer, S., and Leuenberger, M.: Estimation of the fossil-fuel component in atmospheric CO2 based on radiocarbon measurements at the Beromünster tall tower, Switzerland, Atmos. Chem. Phys. Discuss., 2017, 1-33, 2017.

Crosson, E. R. J. A. P. B.: A cavity ring-down analyzer for measuring atmospheric levels of methane, carbon dioxide, and water vapor, 92, 403-408, 2008.

Filges, A., Gerbig, C., Rella, C. W., Hoffnagle, J., Smit, H., Krämer, M., Spelten, N., Rolf, C., Bozóki, Z., Buchholz, B., and Ebert, V.: Evaluation of the IAGOS-Core GHG Package H2O measurements during the DENCHAR airborne inter-comparison campaign in 2011, Atmos. Meas. Tech., 11, 5279–5297, 2018, https://doi.org/10.5194/amt-11-5279-2018. Gao, F., Zhang, X., Zhang, X., Wang, M., and Wang, P.: Virtual electronic nose with diagnosis model for the detection of hydrogen and methane in breath from gastrointestinal bacteria, 28-31 May 2017 2017, 1-3.

Gordon, E., Rothman, S., Hill, C., Kochanov, V., Tan, Y., Bernath, P., Birk, M., Boudon, V., Campargue, A., Chance, K., Drouin, J., Flaud, J., Gamache, R. R., Hodges, J., Jacquemart, D., Perevalov, I., Perrin, A., Shine, P., Smith, M., Tennyson, J., Toon, G., Tran, H., Tyuterev, G., Barbe, A., Császár, G., Devi, M.,

1041   Furtenbacher, T., Harrison, J., Hartmann, J., Jolly, A., Johnson, J., Karman, T., Kleiner, I., Kyuberis, A.

1042   A., Loos, J., Lyulin, M., Massie, S., Mikhailenko, S., Moazzen-Ahmadi, N., Muller, S., Naumenko, O. V.,

1043   Nikitin, A. V., Polyansky, O. L., Rey, M., Rotger, M., Sharpe, S., Sung, K., Starikova, E., Tashkun, S.,

1044   Auwera, J., Wagner, G., Wilzewski, J., Wcisło, P., Yu, S., and Zak, E. J.: The HITRAN2016 molecular

1045   spectroscopic database, 203, 3 - 69, 2017.

1046   Goto, D., Morimoto, S., Ishidoya, S., Aoki, S., and Nakazawa, T.: Terrestrial biospheric and oceanic

1047 CO_2 uptake estimated from long-term measurements of atmospheric CO_2 mole fraction, $\delta 13C$ and

1048 $\delta(O_2/N_2)$ at Ny-Ålesund, Svalbard, Journal of Geophysical Research: Biogeosciences, doi:

1049   10.1002/2017JG003845, 2017. n/a-n/a, 2017.

1050   Gottlieb, K., Le, C. X., Wacher, V., Sliman, J., Cruz, C., Porter, T., and Carter, S.: Selection of a cut-off

1051   for high- and low-methane producers using a spot-methane breath test: results from a large north

1052   American dataset of hydrogen, methane and carbon dioxide measurements in breath, Gastroenterol

1053   Rep, 5, 193-199, 2017.

1054   Hartmann, J.-M., Boulet, C., and Robert, D.: Collisional Effects on Molecular Spectra, Elsevier Science,

1055   2008.

1056   Henne, S., Brunner, D., Folini, D., Solberg, S., Klausen, J., and Buchmann, B.: Assessment of

1057   parameters describing representativeness of air quality in-situ measurement sites, Atmos. Chem.

1058   Phys., 10, 3561-3581, 2010.

1059   Hodges, J. T., Layer, H. P., Miller, W. W., and Scace, G. E.: Frequency-stabilized single-mode cavity

1060   ring-down apparatus for high-resolution absorption spectroscopy, 75, 849-863, 2004.

1061   Keeling, R. F.: Development of an Interferometric Oxygen Analyzer for Precise Measurement of the

1062   Atmospheric O_2 Mole Fraction, UMI, 1988a.

1063   Keeling, R. F.: Measuring correlations between atmospheric oxygen and carbon dioxide mole

1064   fractions: A preliminary study in urban air, J Atmos Chem, 7, 153-176, 1988b.

1065   Keeling, R. F. and Manning, A. C.: 5.15 - Studies of Recent Changes in Atmospheric O2 Content A2 -

1066   Holland, Heinrich D. In: Treatise on Geochemistry (Second Edition), Turekian, K. K. (Ed.), Elsevier,

1067   Oxford, 2014.

1068   Keeling, R. F. and Shertz, S. R.: Seasonal and Interannual Variations in Atmospheric Oxygen and

1069   Implications for the Global Carbon-Cycle, Nature, 358, 723-727, 1992.

1070   Keeling, R. F., Stephens, B. B., Najjar, R. G., Doney, S. C., Archer, D., and Heimann, M.: Seasonal

1071   variations in the atmospheric O-2/N-2 ratio in relation to the kinetics of air-sea gas exchange, Global

1072   Biogeochem Cy, 12, 141-163, 1998.

1073   Lamouroux, J., Sironneau, V., Hodges, J. T., and Hartmann, J. M.: Isolated line shapes of molecular

1074   oxygen: Requantized classical molecular dynamics calculations versus measurements, Physical

1075   Review A, 89, 042504, 2014.

1076   Le Quéré, C., Andrew, R. M., Friedlingstein, P., Sitch, S., Pongratz, J., Manning, A. C., Korsbakken, J. I.,

1077   Peters, G. P., Canadell, J. G., Jackson, R. B., Boden, T. A., Tans, P. P., Andrews, O. D., Arora, V. K.,

1078   Bakker, D. C. E., Barbero, L., Becker, M., Betts, R. A., Bopp, L., Chevallier, F., Chini, L. P., Ciais, P.,

1079   Cosca, C. E., Cross, J., Currie, K., Gasser, T., Harris, I., Hauck, J., Haverd, V., Houghton, R. A., Hunt, C.

1080   W., Hurtt, G., Ilyina, T., Jain, A. K., Kato, E., Kautz, M., Keeling, R. F., Klein Goldewijk, K., Körtzinger, A.,

1081   Landschützer, P., Lefèvre, N., Lenton, A., Lienert, S., Lima, I., Lombardozzi, D., Metzl, N., Millero, F.,

1082   Monteiro, P. M. S., Munro, D. R., Nabel, J. E. M. S., Nakaoka, S. I., Nojiri, Y., Padín, X. A., Peregon, A.,

1083   Pfeil, B., Pierrot, D., Poulter, B., Rehder, G., Reimer, J., Rödenbeck, C., Schwinger, J., Séférian, R.,

1084   Skjelvan, I., Stocker, B. D., Tian, H., Tilbrook, B., van der Laan-Luijkx, I. T., van der Werf, G. R., van

1085   Heuven, S., Viovy, N., Vuichard, N., Walker, A. P., Watson, A. J., Wiltshire, A. J., Zaehle, S., and Zhu,

1086   D.: Global Carbon Budget 2017, Earth Syst. Sci. Data Discuss., 2017, 1-79, 2017.

1087   Machta, L. and Hughes, E.: Atmospheric Oxygen in 1967 to 1970, Science, 168, 3939, 1582-1584,

1088   1970.

1089 Manning, A.: Temporal variability of atmospheric oxygen from both continuos and measurements

1090 and a flask sampling network: tools for studying the global carbon cycle, Ph.D. Ph.D., University of

1091 California, San Diego, San Diego, Calofornia, USA, 2001.

1092 Manning, A. C. and Keeling, R. F.: Global oceanic and land biotic carbon sinks from the Scripps

1093 atmospheric oxygen flask sampling network, Tellus B, 58, 95-116, 2006.

1094 Manning, A. C., Keeling, R. F., and Severinghaus, J. P.: Precise atmospheric oxygen measurements

1095 with a paramagnetic oxygen analyzer, Global Biogeochem Cy, 13, 1107-1115, 1999.

1096 Marrero, T. R. and Mason, E. A.: Gaseous Diffusion Coefficients, Journal of Physical and Chemical

1097 Reference Data 1, 3, 1972.

1098 Martin, N. A., Ferracci, V., Cassidy, N., and Hoffnagle, J. A. J. A. P. B.: The application of a cavity ring-

1099 down spectrometer to measurements of ambient ammonia using traceable primary standard gas

1100 mixtures, 122, 219, 2016.

1101 Mckay, L. F., Eastwood, M. A., and Brydon, W. G.: Methane Excretion in Man - a Study of Breath,

1102 Flatus, and Feces, Gut, 26, 69-74, 1985.

1103 Nevison, C. D., Keeling, R. F., Kahru, M., Manizza, M., Mitchell, B. G., and Cassar, N.: Estimating net

1104 community production in the Southern Ocean based on atmospheric potential oxygen and satellite

1105 ocean color data, Global Biogeochem Cy, 26, 2012.

1106 Oney, B., Henne, S., Gruber, N., Leuenberger, M., Bamberger, I., Eugster, W., and Brunner, D.: The

1107 CarboCount CH sites: characterization of a dense greenhouse gas observation network, Atmos.

1108 Chem. Phys., 15, 11147-11164, 2015.

1109 Press, W. H., Teukolsky, S. A., Vetterling, W. T., and Flannery, B. P.: Numerical Recipes 3rd Edition:

1110 The Art of Scientific Computing, Cambridge Printing Press, Cambridge, England, 1986.

1111 Press, W. H., Teukolsky, S. A., Vetterling, W. T., and Flannery, B. P.: Numerical recipes in C: the art of

1112 scientific computing, Cambridge University Press, London, 1992.

1113 Ryter, S. W. and Choi, A. M. K.: Carbon monoxide in exhaled breath testing and therapeutics, J Breath

1114 Res, 7, 2013.

1115 Satar, E., Berhanu, T. A., Brunner, D., Henne, S., and Leuenberger, M.: Continuous CO2/CH4/CO

1116 measurements (2012–2014) at Beromünster tall tower station in Switzerland, Biogeosciences, 13,

1117 2623-2635, 2016.

1118 Schibig, M. F., Steinbacher, M., Buchmann, B., van der Laan-Luijkx, I. T., van der Laan, S., Ranjan, S.

1119 and Leuenberger, M. C,: Comparison of continuous in situ CO2 observations at Jungfraujoch using

1120 two different measurement techniques, Atmospheric Measurement Techniques

1121 , 8, 57-68, 10.5194/amt-8-57-2015, 2015.

1122 Severinghaus, J. P.: Studies of the terrestrial O2 and carbon cycles in sand dune gases and in

1123 Biosphere Doctoral Ph.D., Columbia University, New York, USA, 1995.

1124 Steig, E. J., Gkinis, V., Schauer, A. J., Schoenemann, S. W., Samek, K., Hoffnagle, J., Dennis, K. J., and

1125 Tan, S. M.: Calibrated high-precision [17]O-excess measurements using cavity ring-down

1126 spectroscopy with laser-current-tuned cavity resonance, Atmos. Meas. Tech., 7, 2014.

1127 Stephens, B. B., Bakwin, P. S., Tans, P. P., Teclaw, R. M., and Baumann, D. D.: Application of a

1128 differential fuel-cell analyzer for measuring atmospheric oxygen variations, J Atmos Ocean Tech, 24,

1129 82-94, 2007.

1130 Sturm, P., Leuenberger, M., Valentino, F.L., Lehmann, B. and B. Ihly: Measurements of CO_2, its stable

1131 isotopes, O_2/N_2, and [222]Rn at Bern, Switzerland, *Atmospheric Chemistry and Physics*, *6*, 1991-2004,

1132 2006.

1133 Tan, Y., Kochanov, R.V., Rothman, L., and Gordon, I.E.:Introduction of water-vapor broadening

1134 coefficients and their temeprature dependence exponents into the HITRAN database, Part 1: CO2,

1135 N2O, CO, CH4, O2, NH3, and H2S, Submitted to Journal of Geophysical Research Atmospheres, 2019,

1136 arXiv:1906.01475 .

1137   Tennyson, J., Bernath, P. F., Campargue, A., Császár, A. G., Daumont, L., Gamache, R. R., Hodges, J. T.,

1138   Lisak, D., Naumenko, O. V., Rothman, L. S., Tran, H., Zobov, N. F., Buldyreva, J., Boone, C. D., De Vizia,

1139   M. D., Gianfrani, L., Hartmann, J.-M., McPheat, R., Weidmann, D., Murray, J., Ngo, N. H., and

1140   Polyansky, O. L.: Recommended isolated-line profile for representing high-resolution spectroscopic

1141   transitions (IUPAC Technical Report), 86, 1931–1943, 2014.

1142   Tohjima, Y.: Method for measuring changes in the atmospheric O-2/N-2 ratio by a gas

1143   chromatograph equipped with a thermal conductivity detector, J Geophys Res-Atmos, 105, 14575-

1144   14584, 2000.

1145   Tran, H., Turbet, M., Hanoufa, S., Landsheere, X., Chelin, P., Ma, Q., Hartmann, J.: The CO_2–

1146   broadened H_2O continuum in the 100–1500 cm-1 region: Measurements, predictions and empirical

1147   model, Journal of Quantitative Spectroscopy and Radiative Transfer, 230, 75-80, 2019.

1148   Valentino, F. L., Leuenberger, M., Uglietti, C., and Sturm, P.: Measurements and trend analysis of O_2,

1149 CO_2 and δ13C of CO_2 from the high altitude research station Junfgraujoch, Switzerland — A

1150   comparison with the observations from the remote site Puy de Dôme, France, Sci Total Environ, 391,

1151   203-210, 2008.

1152   Varghese, P. L. and Hanson, R. K.: Collisional narrowing effects on spectral line shapes measured at

1153   high resolution, Appl. Opt., 23, 2376-2385, 1984.

1154   Wójtewicz, S., Cygan, A., Masłowski, P., Domysławska, J., Wcisło, P., Zaborowski, M., Lisak, D.,

1155   Trawiński, R. S., and Ciuryło, R.: Spectral line-shapes of oxygen B-band transitions measured with

1156   cavity ring-down spectroscopy, Journal of Physics: Conference Series, 548, 012028, 2014.

1157   Wolf, P. G., Parthasarathy, G., Chen, J., O'Connor, H. M., Chia, N., Bharucha, A. E., and Gaskins, H. R.:

1158   Assessing the colonic microbiome, hydrogenogenic and hydrogenotrophic genes, transit and breath

1159   methane in constipation, Neurogastroent Motil, 29, 2017.

1160 Zellweger, C., Forrer, J., Hofer, P., Nyeki, S., Schwarzenbach, B., Weingartner, E., Ammann, M., and

1161 Baltensperger, U.: Partitioning of reactive nitrogen (NO$_y$) and dependence on

1162 meteorological conditions in the lower free troposphere, Atmos. Chem. Phys., 3, 779-796, 2003.

1163